

1

Abstract

2

# Measurement of total hadronic cross sections in the LArIAT experiment

3

4

Elena Gramellini

5

2018

6

Abstract goes here. Limit 750 words.

7  
8

9  
10  
11  
12  
13  
14

15

16

17

18



21

*A mia mamma e mio babbo,*

22

*grazie per le radici e grazie per le ali.*

23

*To my mom and dad,*

24

*thank you for the roots and thank you for the wings.*

# Contents

26	<b>Acknowledgements</b>	<b>vi</b>
27	<b>0 Total Hadronic Cross Section Measurement Methodology</b>	<b>1</b>
28	0.1 Event Selection . . . . .	2
29	0.1.1 Selection of Beamline Events . . . . .	2
30	0.1.2 Particle Identification in the Beamline . . . . .	3
31	0.1.3 TPC Selection: Halo Mitigation . . . . .	3
32	0.1.4 TPC Selection: Shower Removal . . . . .	4
33	0.2 Beamline and TPC Handshake: the Wire Chamber to TPC Match . .	5
34	0.3 The Thin Slice Method . . . . .	7
35	0.3.1 Cross Sections on Thin Target . . . . .	7
36	0.3.2 Not-so-Thin Target: Slicing the Argon . . . . .	8
37	0.3.3 Corrections to the Raw Cross Section . . . . .	10
38	0.4 Procedure testing with truth quantities . . . . .	11
39	<b>1 Data and MC preparation for the Cross Section Measurements</b>	<b>14</b>
40	1.1 Cross Section Analyses Data Sets . . . . .	14
41	1.2 Construction of a Monte Carlo Simulation for LArIAT . . . . .	16
42	1.2.1 G4Beamline . . . . .	16
43	1.2.2 Data Driven MC . . . . .	21
44	1.3 Estimate of Backgrounds in the Pion Cross Section . . . . .	24

45	1.3.1	Background from Pion Capture and Decay . . . . .	24
46	1.3.2	Contributions from the Beamline Background . . . . .	27
47	1.4	Estimate of Energy Loss before the TPC . . . . .	30
48	1.5	Tracking Studies . . . . .	34
49	1.5.1	Angular Resolution . . . . .	34
50	1.6	Calorimetry Studies . . . . .	40
51	1.6.1	Kinetic Energy Measurement . . . . .	40
52	<b>2</b>	<b>Negative Pion Cross Section Measurement</b>	<b>43</b>
53	2.1	Raw Cross Section . . . . .	43
54	2.1.1	Statistical Uncertainty . . . . .	45
55	2.1.2	Treatment of Systematics . . . . .	47
56	2.2	Corrections to the Raw Cross Section . . . . .	48
57	2.2.1	Background subtraction . . . . .	48
58	2.2.2	Efficiency Correction . . . . .	51
59	2.3	Results . . . . .	55
60	<b>3</b>	<b>Positive Kaon Cross Section Measurement</b>	<b>57</b>
61	3.1	Raw Cross Section . . . . .	57
62	<b>A</b>	<b>Additional Tracking Studies for LArIAT Cross Section Analyses</b>	<b>61</b>
63	A.0.1	Study of WC to TPC Match . . . . .	62
64	A.0.2	Tracking Optimization . . . . .	64
65	<b>B</b>	<b>Energy Calibration</b>	<b>65</b>
66	<b>C</b>	<b>Measurement of LArIAT Electric Field</b>	<b>69</b>

# Acknowledgements

*“Dunque io ringrazio tutti quanti.  
Specie la mia mamma che mi ha fatto così funky.”*  
– Articolo 31, Tanqi Funky, 1996 –

*“At last, I thank everyone.  
Especially my mom who made me so funky.”*  
– Articolo 31, Tanqi Funky, 1996 –

A lot of people are awesome, especially you, since you probably agreed to read this when it was a draft.

# Chapter 0

## Total Hadronic Cross Section

## Measurement Methodology

*“Like a lemon to the lime and the bubble to the bee”*

– Eazy-E, Gimmie that \*, 1993 –

This chapter describes the general procedure employed to measure a total hadronic differential cross section in LArIAT. Albeit with small differences, both the  $(\pi^-, \text{Ar})$  and  $(K^+, \text{Ar})$  total hadronic cross section measurements rely on the same procedure. We start by selecting the particle of interest using a combination of beamline detectors and TPC information (Section 0.1). We then perform a handshake between the beamline information and the TPC tracking to assure the selection of the correct TPC track (Section 0.2). Finally, we apply the “thin slice” method and measure the “raw” hadronic cross section (Section 0.3). A series of corrections are then evaluated to obtain the “true” cross section (Section 0.3.3).

At the end of this chapter, we show a sanity check of the methodology by applying the thin slice method employing only MC truth information and retrieving the Geant4 tabulated cross section for pions and kaons (Section 0.4).



## 0.1 Event Selection

The measurement of the  $(\pi^-, \text{Ar})$  and  $(K^+, \text{Ar})$  total hadronic cross section in LArIAT starts by selecting the pool of pion or kaon candidates and measuring their momentum. This is done through the series of selections on beamline and TPC information described in the next sections. The summary of the event selection in data is reported in Table 1.

### 0.1.1 Selection of Beamline Events

As shown in equation 5, we leverage the beamline particle identification and momentum measurement before entering the TPC as an input to evaluate the kinetic energy for the hadrons used in the cross sections measurements. Thus, we select the LArIAT data to keep only events whose wire chamber and time of flight information is registered (line 1 in in Table 1). Additionally, we perform a check of the plausibility of the trajectory inside the beamline detectors: given the position of the hits in the four wire chambers, we make sure the particle's trajectory does not cross any impenetrable material such as the collimator and the magnets steel (line 2 in in Table 1).

	Run-II Neg Pol	Run-II Pos Pol
1. Events Reconstructed in Beamline	158396	260810
2. Events with Plausible Trajectory	147468	240954
3. Beamline $\pi^-/\mu^-/e^-$ Candidate	138481	N.A.
4. Beamline $K^+$ Candidate	N.A	2837
5. Events Surviving Pile Up Filter	108929	2389
6. Events with WC2TPC Match	41757	1081
7. Events Surviving Shower Filter	40841	N.A.
8. Available Events For Cross Section	40841	1081

Table 1: Number of data events for Run-II Negative and Positive polarity

### 108 **0.1.2 Particle Identification in the Beamline**

109 In data, the main tool to establish the identity of the hadron of interest is the LArIAT  
 110 tertiary beamline, in its function of mass spectrometer. We combine the measurement  
 111 of the time of flight,  $TOF$ , and the beamline momentum,  $p_{Beam}$ , to reconstruct the  
 112 invariant mass of the particles in the beamline,  $m_{Beam}$ , as follows

$$m_{Beam} = \frac{p_{Beam}}{c} \sqrt{\left(\frac{TOF * c}{l}\right)^2 - 1}, \quad (1)$$

113 where  $c$  is the speed of light and  $l$  is the length of the particle's trajectory between  
 114 the time of flight paddels.

115 Figure 1 shows the mass distribution for the Run II negative polarity runs on the  
 116 left and positive polarity runs on the right. We perform the classification of events  
 117 into the different samples as follows:

- 118 •  $\pi/\mu/e$ : mass < 350 MeV/c<sup>2</sup>
- 119 • kaon: 350 MeV < mass < 650 MeV/c<sup>2</sup>
- 120 • proton: 650 MeV < mass < 3000 MeV/c<sup>2</sup>.

121 Lines 3 and 4 in in Table 1 show the number of negative  $\pi/\mu/e$  and positive  $K$   
 122 candidates which pass the mass selection for LArIAT Run-II data.

### 123 **0.1.3 TPC Selection: Halo Mitigation**

124 The secondary beam impinging on LArIAT secondary target produces a plethora of  
 125 particles which propagates downstream. The presence of upstream and downstream  
 126 collimators greatly abates the number of particles tracing down the LArIAT tertiary  
 127 beamline. However, it is possible that more than one particle sneaks into the LArTPC  
 128 during its readout time: the TPC readout is triggered by the particle firing the

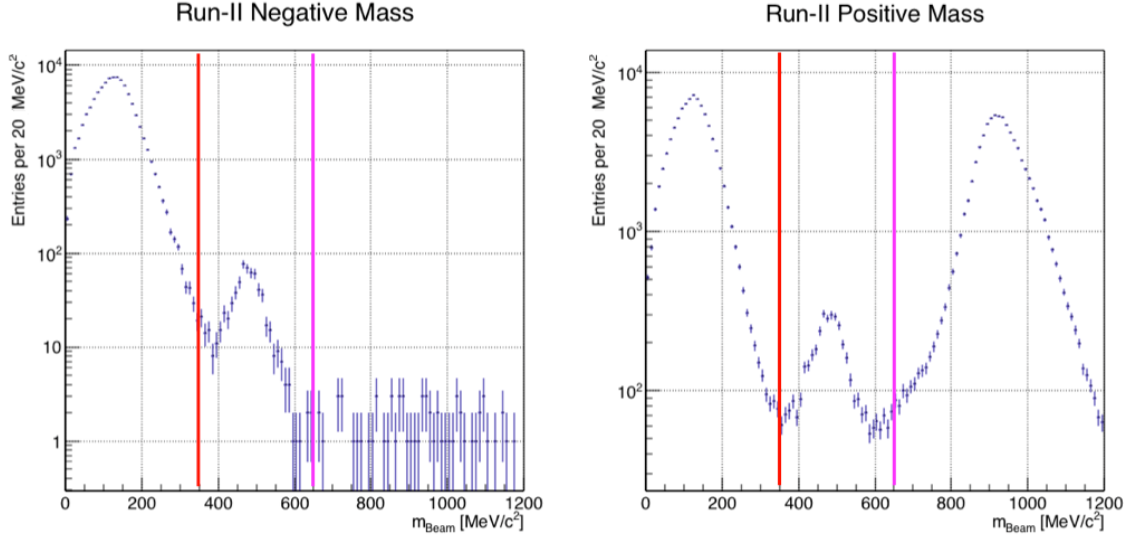


Figure 1: Distribution of the beamline mass as calculated according to equation 1 for the Run-II events reconstructed in the beamline, negative polarity runs on the left and positive polarity runs on the right. The classification of the events into  $\pi^\pm/\mu^\pm/e^\pm$ ,  $K^\pm$ , or (anti)proton is based on these distributions, whose selection cut are represented by the vertical colored lines.

beamline detectors, but particles from the beam halo might be present in the TPC at the same time. We call “pile up” the additional traces in the TPC. We adjusted the primary beam intensity between LArIAT Run I and Run II to reduce the presence of events with high pile up particles in the data sample. For the cross section analyses, we remove events with more than 4 tracks in the first 14 cm upstream portion of the TPC from the sample (line 5 in in Table 1).

#### 0.1.4 TPC Selection: Shower Removal

In the case of the  $(\pi^-, \text{Ar})$  cross section, the resolution of beamline mass spectrometer is not sufficient to select a beam of pure pions. In fact, muons and electrons survive the selection on the beamline mass. It is important to notice that the composition of the negative polarity beam is mostly pions, as will be discussed in section 1.2.1. Still, we devise a selection on the TPC information to mitigate the presence of electrons

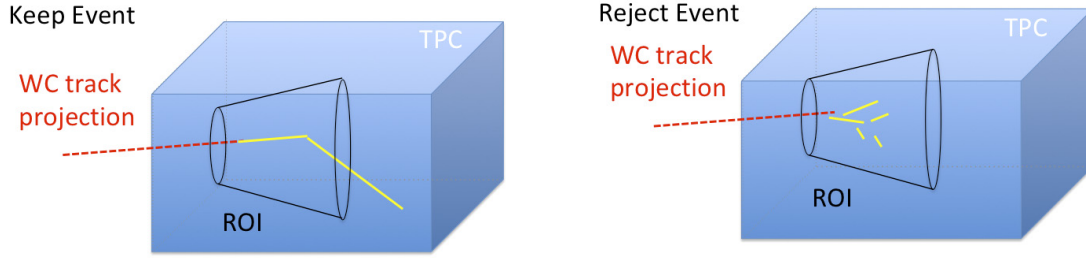


Figure 2: Visual rendering of the shower filter. The ROI is a cut cone, with a small radius of 4 cm, a big radius of 10 cm and an height of 42 cm (corresponding to 3 radiation lengths for electrons in Argon).

141 in the sample used for the pion cross section. The selection relies on the different  
 142 topologies of a pion and an electron event in the argon: while the former will trace  
 143 a track inside the TPC active volume, the latter will tend to “shower”, i.e. interact  
 144 with the medium, producing bremsstrahlung photons which pair convert into several  
 145 short tracks. In order to remove the shower topology, we create a region of interest  
 146 (ROI) around the TPC track corresponding to the beamline particle. We look for  
 147 short tracks contained in the ROI, as depicted in figure 4: if more then 5 tracks  
 148 shorter than 10 cm are in the ROI, we reject the event. Line 7 in in Table 1 shows  
 149 the number of events surviving this selection.

## 150 0.2 Beamline and TPC Handshake: the Wire Cham- 151 ber to TPC Match

152 For each event passing the selection on its beamline information, we need to identify  
 153 the track inside the TPC corresponding to the particle which triggered the beamline  
 154 detectors, a procedure we refer to as “WC to TPC match” (WC2TPC for short).  
 155 In general, the TPC tracking algorithm will reconstruct more than one track in the  
 156 event, partially due to the fact that hadrons interact in the chamber and partially  
 157 because of pile up particles during the triggered TPC readout time, as shown in

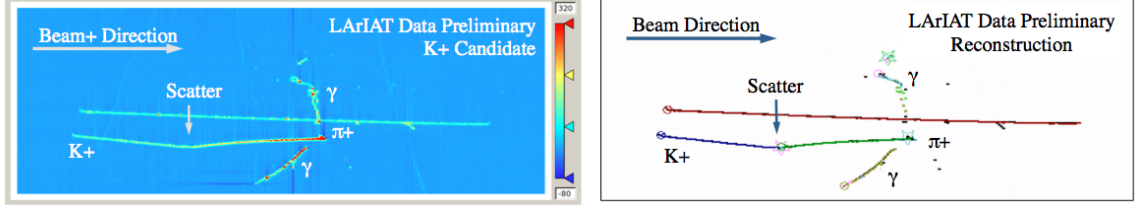


Figure 3: Kaon candidate event: on the right, event display showing raw quantities; on the left, event display showing reconstructed tracks. In the reconstructed event display, different colors represent different track objects. A kink is visible in the kaon ionization, signature of a hadronic interaction: the tracking correctly stops at the kink position and two tracks are formed. An additional pile-up track is so present in the event (top track in red).

figure 3.

We attempt to uniquely match one wire chamber track to one and only one reconstructed TPC track. In order to determine if a match is present, we apply a geometrical selection on the relative the position of the wire chamber and TPC tracks. We start by considering only TPC tracks whose first point is in the first 2 cm upstream portion of the TPC for the match. We project the wire chamber track to the TPC front face where we define the coordinates of the projected point as  $x_{FF}$  and  $y_{FF}$ . For each considered TPC track, we define  $\Delta X$  as the difference between the  $x$  position of the most upstream point of the TPC track and  $x_{FF}$ .  $\Delta Y$  is defined analogously. We define the radius difference,  $\Delta R$ , as  $\Delta R = \sqrt{\Delta X^2 + \Delta Y^2}$ . We define as  $\alpha$  the angle between the incident WC track and the TPC track in the plane that contains them. If  $\Delta R < 4$  cm,  $\alpha < 8^\circ$ , a match between WC-track and TPC track is found. We describe how we determine the value for the radius and angular selection in Section A.0.1. We discard events with multiple WC2TPC matches. We use only those TPC tracks that are matched to WC tracks in the cross section calculation. Line 6 in Table 1 shows the number of events where a unique WC2TPC match was found.

In MC, we mimic the matching between the WC and the TPC track by constructing a fake WC track using truth information at wire chamber four. We then apply the same WC to TPC matching algorithm as in data.

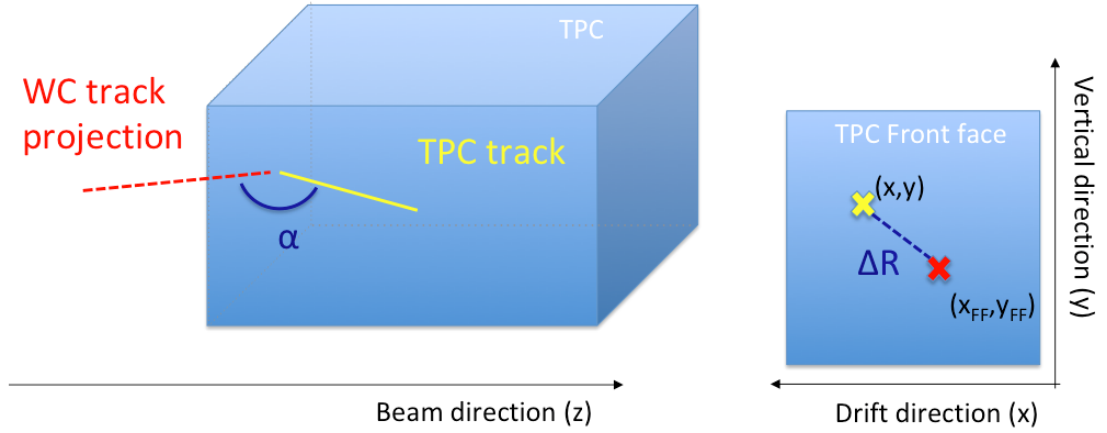


Figure 4: Visual rendering of the wire chamber to TPC match.

### 0.3 The Thin Slice Method

Once we have selected the pool of hadron candidates and we have identified the TPC track corresponding to the beamline event, we apply the thin slice method to measure the cross section, as the following sections describe.

#### 0.3.1 Cross Sections on Thin Target

Cross section measurements on a thin target have been the bread and butter of nuclear and particle experimentalists since the Geiger-Marsden experiments [66]. At their core, this type of experiments consists in shooting a beam of particles with a known flux on a thin slab of material and recording the outgoing flux.

In general even in the case of thin target, the target is not a single particle, but rather a slab of material containing many diffusion centers. The so-called “thin target” approximation assumes that the target centers are uniformly distributed in the material and that the target is thin compared to the projectile interaction length, so that no center of interaction sits in front of another. In this approximation, the ratio between the number of particles interacting in the target  $N_{\text{Int}}$  and the number of incident particles  $N_{\text{Inc}}$  on the target determines the interaction probability  $P_{\text{Interacting}}$ ,

193 which is the complementary to one of the survival probability  $P_{Survival}$ . Equation 2

$$P_{Survival} = 1 - P_{Interacting} = 1 - \frac{N_{Int}}{N_{Inc}} = e^{-\sigma_{TOT}n\delta X} \quad (2)$$

194 describes the probability for a particle to survive the thin target. This formula relates  
 195 the interaction probability to the total hadronic cross section ( $\sigma_{TOT}$ ), the density of  
 196 the target centers ( $n$ )<sup>1</sup> and the thickness of the target along the incident hadron  
 197 direction ( $\delta X$ ). If the target is thin compared to the interaction length of the process  
 198 considered, we can Taylor expand the exponential function in equation 2 and find  
 199 a simple proportionality relationship between the cross section and the number of  
 200 incident and interacting particles, as shown in equation 3:

$$1 - \frac{N_{Int}}{N_{Inc}} = 1 - \sigma_{TOT}n\delta X + O(\delta X^2). \quad (3)$$

201 Solving for the cross section, we find:

$$\sigma_{TOT} = \frac{1}{n\delta X} \frac{N_{Int}}{N_{Inc}}. \quad (4)$$

### 202 **0.3.2 Not-so-Thin Target: Slicing the Argon**

203 The interaction length of pions and kaons in argon is expected to be of the order  
 204 of 50 cm for pions and 100 cm for kaons. Thus, the LArIAT TPC, with its 90 cm  
 205 of length, is not a thin target. However, the fine-grained tracking of the LArIAT  
 206 LArTPC allows us to treat the argon volume as a sequence of many adjacent thin  
 207 targets.

208 As described in Chapter ??, LArIAT wire planes consist of 240 wires each. The  
 209 wires are oriented at +/- 60° from the vertical direction at 4 mm spacing, while the

---

1. The scattering center density in the target,  $n$ , relates to the argon density  $\rho$ , the Avogadro number  $N_A$  and the argon molar mass  $m_A$  as  $n = \frac{\rho N_A}{m_A}$ .

beam direction is oriented 3 degrees off the  $z$  axis in the  $XZ$  plane. The wires collect signals proportional to the energy loss of the hadron along its path in a  $\delta X = 4$  mm/ $(\sin(60^\circ)\cos(3^\circ)) \approx 4.7$  mm slab of liquid argon. Thus, one can think to slice the TPC into many thin targets of  $\delta X = 4.7$  mm thickness along the direction of the incident particle, making a measurement at each wire along the path.

Considering each slice  $j$  a “thin target”, we can apply the cross section calculation from Equation 4 iteratively, evaluating the kinetic energy of the hadron as it enters each slice,  $E_j^{kin}$ . For each WC2TPC matched particle, the energy of the hadron entering the TPC is known thanks to the momentum and mass determination by the tertiary beamline,

$$E_{FrontFace}^{kin} = \sqrt{p_{Beam}^2 - m_{Beam}^2} - m_{Beam} - E_{loss}, \quad (5)$$

where  $E_{loss}$  is a correction for the energy loss in the uninstrumented material between the beamline and the TPC front face. The energy of the hadron at each slab is determined by subtracting the energy released by the particle in the previous slabs. For example, at the  $j^{th}$  point of a track, the kinetic energy will be

$$E_j^{kin} = E_{FrontFace}^{kin} - \sum_{i < j} E_{Dep,i}, \quad (6)$$

where  $E_{Dep,i}$  is the energy deposited at each argon slice before the  $j^{th}$  point as measured by the calorimetry associated with the tracking.

If the particle enters a slice, it contributes to  $N_{Inc}(E^{kin})$  in the energy bin corresponding to its kinetic energy in that slice. If it interacts in the slice, it also contributes to  $N_{Int}(E^{kin})$  in the appropriate energy bin. The cross section as a function of kinetic energy,  $\sigma_{TOT}(E^{kin})$  will then be proportional to the ratio  $\frac{N_{Int}(E^{kin})}{N_{Inc}(E^{kin})}$ .

Our goal is to measure the total interaction cross section, independently from the topology of the interaction. Thus, we determine that a hadron interacted simply by



	min	max
$X$	1 cm	46 cm
$Y$	-15 cm	15 cm
$Z$	0 cm	86 cm

Table 2: Fiducial volume boundaries used to determine cross section interaction point.

232 requiring that the last point of the WC2TPC matched track lies inside the fiducial  
 233 volume, whose boundaries are defined in Table 2. If the TPC track stops within  
 234 the fiducial volume, its last point will be the interaction point; if the track crosses  
 235 the boundaries of the fiducial volume, the track will be considered “through going”  
 236 and no interaction point will be found. The only points of the hadronic candidate  
 237 track considered to fill the  $N_{\text{Inc}}$  and  $N_{\text{Inc}}$  plots are the ones contained in the fiducial  
 238 volume.

### 239 0.3.3 Corrections to the Raw Cross Section

240 Equation 4 is a prescription for measuring the cross section in case of a pure beam  
 241 of the hadron of interest and 100% efficiency in the determination of the interaction  
 242 point. For example, if LArIAT had a beam of pure pions and were 100% efficient  
 243 in determining the interaction point within the TPC, the pion cross section in each  
 244 energy bin would be given by

$$\sigma_{TOT}^{\pi^-}(E_i) = \frac{1}{n\delta X} \frac{N_{\text{Int}}^{\pi^-}(E_i)}{N_{\text{Inc}}^{\pi^-}(E_i)}. \quad (7)$$

245 Unfortunately, this is not the case. In fact, the selection used to isolate pions  
 246 in the LArIAT beam allows for the presence of some muons and electrons as back-  
 247 ground, while the kaon selection allows for a small percentage of protons (see Section  
 248 1.2.1). Also, the LArIAT TPC is not 100% efficient in determining the interaction  
 249 point. Therefore we need to apply two corrections evaluated on the MC in order to  
 250 extract the true cross section from LArIAT data: the background subtraction and

the efficiency correction. Still using the pion case as example, we estimate the pion cross section in each energy bin changing Equation 7 into

$$\sigma_{TOT}^{\pi^-}(E_i) = \frac{1}{n\delta X} \frac{N_{Int}^{\pi^-}(E_i)}{N_{Inc}^{\pi^-}(E_i)} = \frac{1}{n\delta X} \frac{\epsilon^{Inc}(E_i)[N_{Int}^{TOT}(E_i) - B_{Int}(E_i)]}{\epsilon^{Int}(E_i)[N_{Inc}^{TOT}(E_i) - B_{Inc}(E_i)]}, \quad (8)$$

where  $N_{Int}^{TOT}(E_i)$  and  $N_{Incident}^{TOT}(E_i)$  is the measured content of the interacting and incident histograms for events that pass the event selection,  $B_{Int}(E_i)$  and  $B_{Inc}(E_i)$  represent the contributions from the background to the interacting and incident histograms respectively, and  $\epsilon^{Int}(E_i)$  and  $\epsilon^{Inc}(E_i)$  are the efficiency corrections for said histograms.

As we will show in section 1.3, the background subtraction for the interacting and incident histograms can be translated into a corresponding relative pion content  $C_{Interacting}^{\pi MC}(E_i)$  and  $C_{Incident}^{\pi MC}(E_i)$  and the cross section re-written as follows

$$\sigma_{TOT}^{\pi^-}(E_i) = \frac{1}{n\delta X} \frac{\epsilon^{Inc}(E_i)}{\epsilon^{Int}(E_i)} \frac{C_{Int}^{\pi MC}(E_i)}{C_{Inc}^{\pi MC}(E_i)} \frac{N_{Int}^{TOT}(E_i)}{N_{Inc}^{TOT}(E_i)}. \quad (9)$$

## 0.4 Procedure testing with truth quantities

The  $(\pi^-, Ar)$  and  $(K^+, Ar)$  total hadronic cross section implemented in Geant4 can be used as a tool to validate the measurement methodology. We describe here a closure test done on Monte Carlo to prove that the methodology of slicing the TPC retrieves the underlying cross section distribution implemented in Geant4 within the statistical uncertainty.

For pions and kaons in the considered energy range, the Geant4 inelastic model adopted is “BertiniCascade”; the pion elastic cross sections are tabulated from on Chips, while the kaon elastic cross sections are tabulated on Gheisha and Chips.

For the validation test, we fire a sample of pions and a sample of kaons inside the LArIAT TPC active volume using the Data Driven Monte Carlo (see section 1.2.2).

272 We apply the thin-sliced method using only true quantities to calculate the hadron  
 273 kinetic energy at each slab in order to decouple reconstruction effects from possible  
 274 issues with the methodology. For each slab of 4.7 mm length along the path of the  
 275 hadron, we integrate the true energy deposition as given by the Geant4 transportation  
 276 model. Then, we recursively subtracted it from the hadron kinetic energy at the TPC  
 277 front face to evaluate the kinetic energy at each slab until the true interaction point is  
 278 reached. Since the MC is a pure beam of the hadron of interest and truth information  
 279 is used to retrieve the interaction point, no correction is applied. Doing so, we obtain  
 280 the true interacting and incident distributions for the considered hadron, from which  
 281 we derive the true MC cross section as a function of the hadron true kinetic energy.

282 Figure 5 shows the total hadronic cross section for argon implemented in Geant4  
 283 10.03.p1 (solid lines) overlaid with the true MC cross section as obtained with the  
 284 sliced TPC method (markers) for pions on the left and kaons on the right; the total  
 285 cross section is shown in green, the elastic cross section in blue and the inelastic  
 286 cross section in red. The nice agreement with the Geant4 distribution and the cross  
 287 section obtained with the sliced TPC method gives us confidence in the validity of  
 288 the methodology.

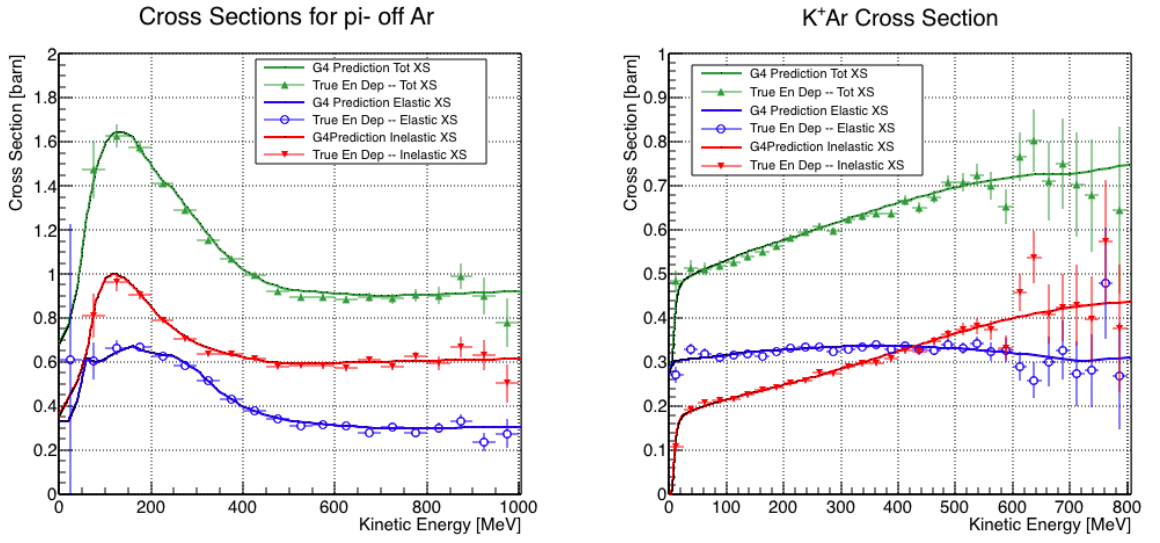


Figure 5: Hadronic cross sections for  $(\pi^-, \text{Ar})$  on the left and  $(K^+, \text{Ar})$  on the right as implemented in Geant4 10.03.p1 (solid lines) overlaid the true MC cross section as obtained with the sliced TPC method (markers). The total cross section is shown in green, the elastic cross section in blue and the inelastic cross section in red.

# Chapter 1

## Data and MC preparation for the Cross Section Measurements

*“Il dolce non lo mangi mai, ma qualche volta ti rifai.*

*Abbracciami”*

– Pietro Ciampi, L’amore e’ tutto qui, 1971 –

This chapter describes the work done on the data and Monte Carlo samples in preparation for the cross section analyses. This entails the choice of the datasets and the production of the information needed to construct the Monte Carlo Simulation (Section 1.1), the construction and use of said Monte Carlo simulation (section 1.2), the study of backgrounds for the pion cross section (Section 1.3), the study of the energy loss between WC4 and TPC (Section 1.4), the study of the tracking in the TPC (Section 1.5), and study of the calorimetry response (Section 1.6).

### 1.1 Cross Section Analyses Data Sets

We choose LArIAT Run-II as the data period for the  $(\pi^-, \text{Ar})$  and  $(K^+, \text{Ar})$  total hadronic cross section analyses. Data taking for the this period started on 03/15/2016

and ended on 07/31/2016. Since we are interested in beamline and TPC information, we ask basic requirements on the operational status of the time of flight, wire chambers and TPC to form the good run list for this period, which we informally call “lovely runs”.

The subset of lovely runs chosen for the  $(\pi^-, \text{Ar})$  total hadronic cross section analysis includes only the -60A and -100A magnet configurations in negative polarity, even if LArIAT explored several other beamline configurations during Run-II. The -60A and -100A combined data set accounts for approximately 90% of the total Run-II negative polarity runs. The choice of the main two beamline settings limits the need for the production of many different MC sets and related corrections, still maintaining a high number of events.

Similarly, the subset of lovely runs chosen for the  $(K^+, \text{Ar})$  total hadronic cross section analysis includes only the +60A and +100A magnet configurations in positive polarity. It should be noted that kaons are extremely rare in the +60A sample, thus the data sample for the  $(K^+, \text{Ar})$  cross section after the mass selection is about 90% +100A runs, as shown in Table 1.1.

For the first measurements in LArIAT that uses both beamline and TPC information, we choose strict requirements on the reconstruction of the WC tracks, the so-called “Picky Track” sample (see Section ??). This choice presents two advantages: the uncertainty on the momentum reconstruction for the “Picky Tracks” sample is smaller compared to the “High Yield” sample, and the comparison with the beamline MC results is straightforward. A possible future update and cross check of these analysis would be the use of the High Yield sample, where the statistics is about three times higher.

The breakdown of beamline events as a function of the magnets settings is shown in Table 1.1. The choice of the data sets determines the production of beamline MC and serves as basis for the production of Data Driven MC, as shown in the next

sections.

## 1.2 Construction of a Monte Carlo Simulation for LArIAT

For the simulation of LArIAT events and for the simulation of the datasets' particle make up, we use a combination of two MC generators: the G4Beamline Monte Carlo and the Data Driven single particle Monte Carlo (DDMC). We use the G4Beamline MC to simulate the particle transportation in the beamline and calculate the particle composition of the beam just after the fourth Wire Chamber (WC4). In order to simulate the beamline particles after WC4 and in the TPC, we use the DDMC.

### 1.2.1 G4Beamline

G4Beamline simulates the beam collision with the LArIAT secondary target, the energy deposited by the particles in the LArIAT beamline detectors, and the action of the LArIAT magnets, effectively accounting for particle transportation through the beamline from the LArIAT target until “Big Disk”, a fictional, void detector located just before the LArIAT cryostat. At the moment of this writing, G4Beamline does not simulated the responses of the beamline detectors. It is possible to interrogate the truth level information of the simulated particles in several points of the geometry. In order to ease the handshake between G4Beamline and the DDMC, we ask for the beam composition just after WC4. Since LArIAT data are taken under different

	I = 60 A	I = 100 A	Total
Data Events after $\pi/\mu/e$ Mass Selection	67068	71413	138481
Data Events after $K$ Mass Selection	274	2563	2837

Table 1.1: Number of data events which fit the  $\pi/\mu/e$  or  $K$  mass hypothesis as a function of magnet settings.

beam conditions, we need to simulate separately the beam composition according to the magnets' settings and the secondary beam intensity with G4Beamline. For the pion cross section analysis the relevant beam conditions are secondary beam energy of 64 GeV, negative polarity magnet with current of 100 A and 60 A. For the kaon cross section analysis the relevant beam conditions is a secondary beam energy of 64 GeV, positive polarity magnet with current of 100 A.

### Beam Composition for Negative Pion Cross Section

Even if pions are by far the biggest beam component in negative polarity runs, the LArIAT tertiary beam is not a pure pion beam. While useful to discriminate between pions, kaons, and protons, the beamline detectors are not sensitive enough to discriminate among the lighter particles in the beam: electrons, muons and pions fall under the same mass hypothesis. Thus, we need to assess the contamination from beamline particles other than pions in the event selections used for the pion cross section analysis and correct for its effects. The first step of this process is assessing the percentage of electrons and muons in the  $\pi/\mu/e$  beamline candidates via the G4Beamline MC. Since the beamline composition is a function of the magnet settings, we simulate separately events for magnet current of -60A and -100A. Figure 1.1 shows the momentum predictions from G4Beamline overlaid with data for the 60A runs (left) and for the 100A runs (right). The predictions for electrons, muons and pions have been staggered and their sum is area normalized to data. Albeit not perfect, these plots show a reasonable agreement between the momentum shapes in data and MC. We attribute the difference in shape to a two approximations performed in the MC. Firstly, G4Beamline lacks the simulation of the WC efficiency which is momentum dependent and leads to enhance the number events in the center of the momentum distribution. Secondly, G4Beamline stop tracking pions and their products if they decay in after WC1; in data, pion decays in flight can still create a



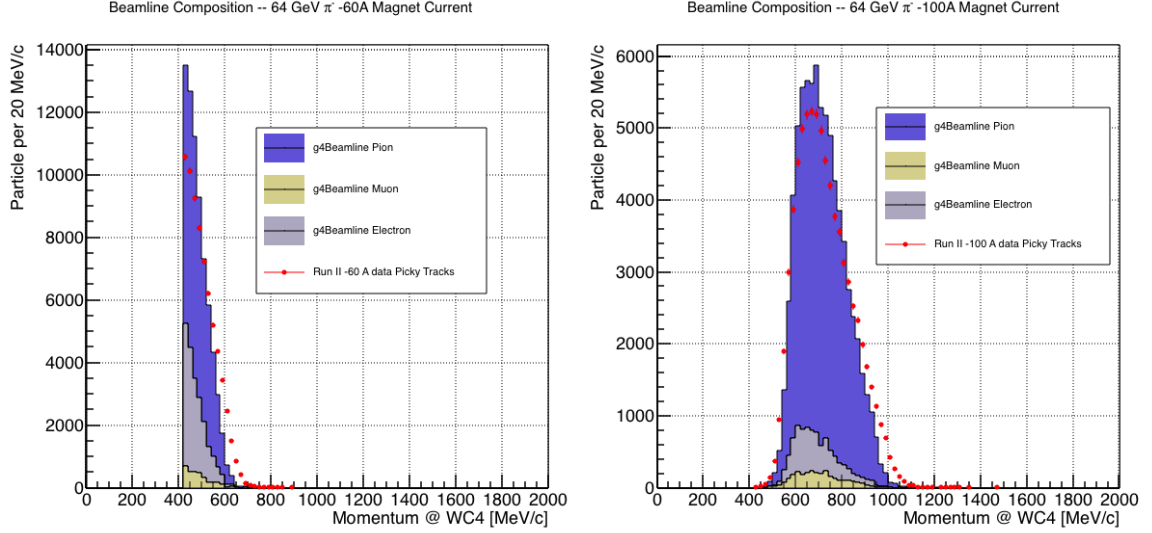


Figure 1.1: Beam composition for the -60A runs (left) and -100A runs (right). The solid blue plot represents the simulated pion content, the yellow plot represents the simulated muon content and the grey plot represents the simulated electron content. The plots are area normalized to the number of data events, shown in red.

	I = -60 A	I = -100 A
G4Pions	68.8 %	87.4 %
G4Muons	4.6 %	3.7 %
G4Electrons	26.6 %	8.9 %

Table 1.2: Simulated beamline composition per magnet settings

tigger if the produced muon travels thought the beamline detectors. In the pion cross  
section analysis, these differences between data and G4Beamline are accounted for as  
a systematic uncertainty related to the beam composition (see Section 2.2.1).

Table 1.2 shows the beam composition per magnet setting after the mass selection  
according to the G4Beamline simulation.

The estimated beam composition is used as a basis to estimate the background  
contamination in the  $(\pi^-, \text{Ar})$  cross section measurement, whose full treatment is  
described in section 1.3.

## 385 Beam Composition for Positive Kaon Cross Section

386 In the positive polarity runs, the tertiary beam composition is mainly pions and  
387 protons. The left side of Figure 1.2 shows the predictions for the momentum spectra  
388 for the 100A positive runs according to G4Beamline (solid colors) overlaid with data  
389 (black points). Since the LArIAT beamline detectors can discriminate between kaons  
390 and other particles, we do not rely on the G4Beamline simulation to estimate the  
391 beamline contamination in the pool of kaon candidates (as in the case of the pion  
392 cross section), but rather we use a data drive approach. The basic idea of this data  
393 driven approach is to estimate the bleed over from high and low mass peaks under  
394 the kaon peak by fitting the tails of the  $\pi/\mu/e$  and proton mass distributions, as  
395 shown in Figure 1.2 right side. Since the shape of the tails is unknown, the estimate  
396 is done multiple times varying the range and shape for reasonable functions. For  
397 example, to estimate the proton content under the kaon peak, we start by fitting the  
398 left tail of the proton mass distribution with a gaussian function between  $650 \text{ MeV}/c^2$   
399 and  $750 \text{ MeV}/c^2$ . We extend the fit function under the kaon peak and integrate the  
400 extended fit function between  $350\text{-}650 \text{ MeV}/c^2$ . We integrate the mass histogram  
401 in the same range and calculate the proton contamination as the ratio between the  
402 two integrals. We repeat this procedure for several fit shapes (gaussian, linear and  
403 exponential functions) and tail ranges. Finally, we calculate the contamination as  
404 the weighted average of single estimates, where the weights are calculated to be the  
405  $1./|1 - \chi^2|$  of the tail fits. The procedure is repeated for lighter particles mass peak  
406 independently. With 12 iterations of this method we find a proton contamination of  
407  $5.0 \pm 2.0 \%$  and a contamination from the lighter particles of  $0.2 \pm 0.5 \%$ . The  
408 estimate of the proton background is currently not used in the kaon cross section  
409 analysis, but it is a fundamental step to retrieve the true kaon cross section which  
410 will be implemented in the further development of the analysis.

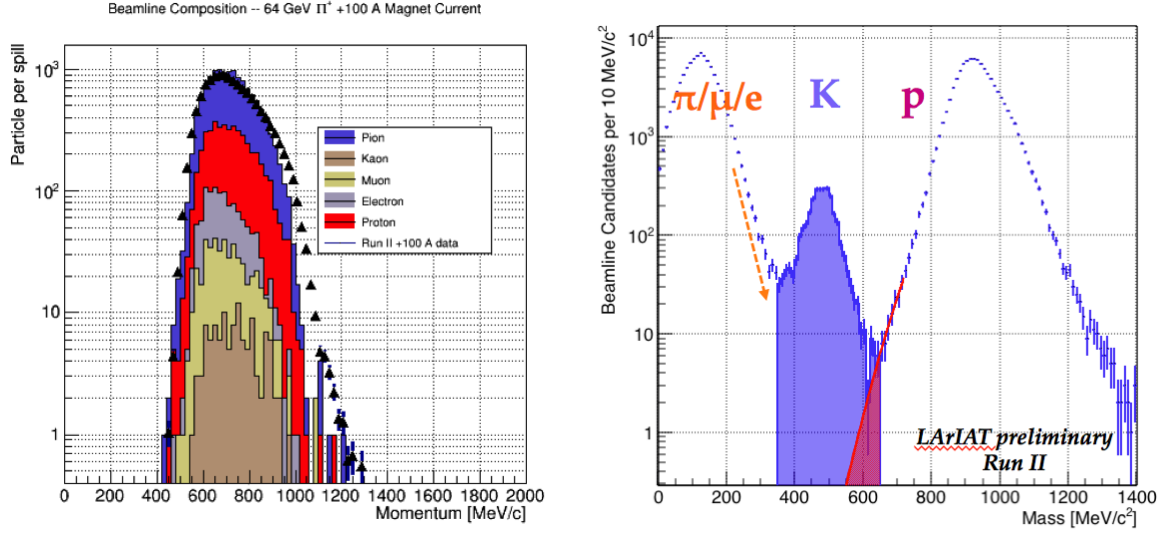


Figure 1.2: *Left:* Beam composition for the +100A runs after WC4 (no mass selection applied). The solid colors represent the contributions from the G4Beamline simulated particles: blue plot represents the simulated pion content, the yellow plot represents the simulated muon content and the grey plot represents the simulated positron content, the red the proton content and the mustard the kaon content. The plots are area normalized to the number of data events, shown in black. *Right:* Mass distribution for the Run-II positive runs, where the area under the kaon mass peak is highlighted in purple. The area under the extension of a possible fit for the proton tail is highlighted in red.

### 1.2.2 Data Driven MC

The Data Driven single particle Monte Carlo (DDMC) is a single particle gun which simulates the particle transportation from WC4 into the TPC leveraging on the beam-line data information. The DDMC uses the data momentum and position at WC4 to derive the event generation: a general sketch of the DDMC workflow is shown in Figure 1.3.

When producing a DDMC sample, beamline data from a particular running period and/or running condition are selected first. For example, data for the negative 60A runs and for the negative 100A runs inform the event generation stage of two different DDMC samples. Figure 1.4 schematically shows the data quantities of interest leveraged from data: the momentum ( $P_x, P_y, P_z$ ) and position ( $X, Y$ ) at WC4. For each data event, we obtain the particle position ( $X, Y$ ) at WC4 directly from the data measurement; we calculate the components of the momentum using the beam-line measurement of the momentum magnitude in conjunction with the hits on WC3 and WC4 to determine the direction of the momentum vector, as described in section ???. The momentum and position of the selected data form a 5-dimensional tuple, which we sample thousands of times through a 5-dimensional hit-or-miss sampling procedure to generate the MC events. This sampling generates MC events with the same momentum and position distributions as data, with the additional benefit of accounting for the correlations between the  $P_x, P_y, P_z, X, Y$  variables. As an example, the results of the DDMC generation compared to data for the kaon +100A sample are shown in figure 1.5 for the  $P_z, X$  and  $Y$  distributions; as expected, MC and data agree within the statistical uncertainty by construction. A LArSoft simulation module then launches single particle MC from  $z = -100$  cm (the location of the WC4) using the generated events. The particles are free to decay and interact in their path from WC4 to the TPC according to the Geant4 simulation.

Using the DDMC technique ensures that the MC and data particles have very

438 similar momentum, position and angular distributions at WC4 and allows us to use  
 439 the MC sample in several occasions: to estimate the background contamination to  
 440 the pion cross section (see Section 1.3), to calibrate the energy loss upstream of the  
 441 TPC (see Section 1.4), or to study the tracking and the calorimetric performance  
 442 (sections 1.5 and 1.6). A small caveat is in order here: the DDMC is a single particle  
 443 Monte Carlo, which means that the beam pile-up is not simulated.

444 We generate six samples for the pion cross section measurement: three samples  
 445 of  $\sim 330000$  pions, muons and electrons to simulate the negative 60A runs, and three  
 446 samples of  $\sim 340000$  pions, muons and electrons for the negative 100A runs. We  
 447 generate a sample of 195000 kaons for the kaon cross section analysis.

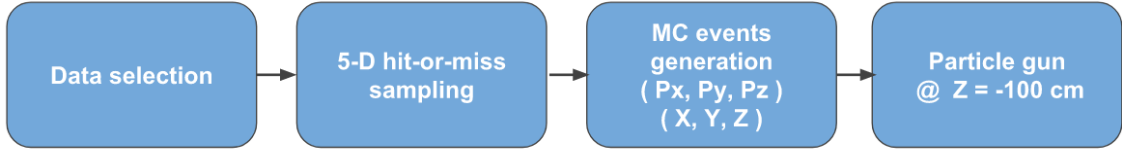


Figure 1.3: Workflow for Data Driven single particle Monte Carlo production.

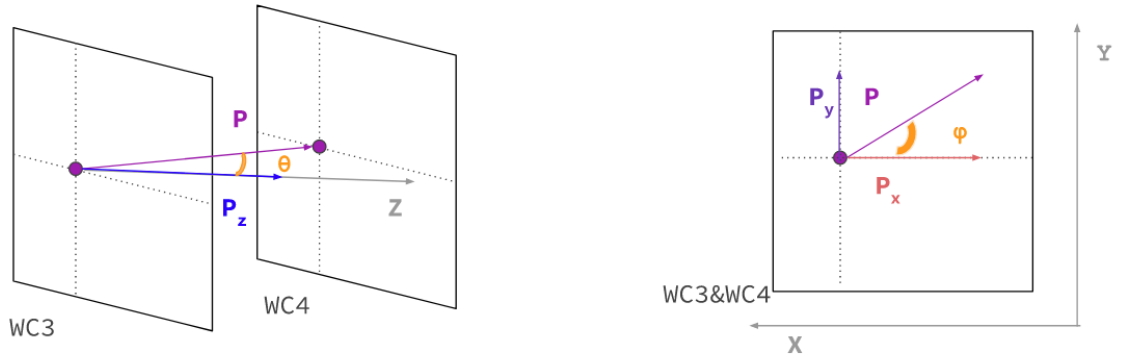


Figure 1.4: Scheme of the quantities of interest for the DDMC event generation:  $P_x, P_y, P_z, X, Y$  at WC4.

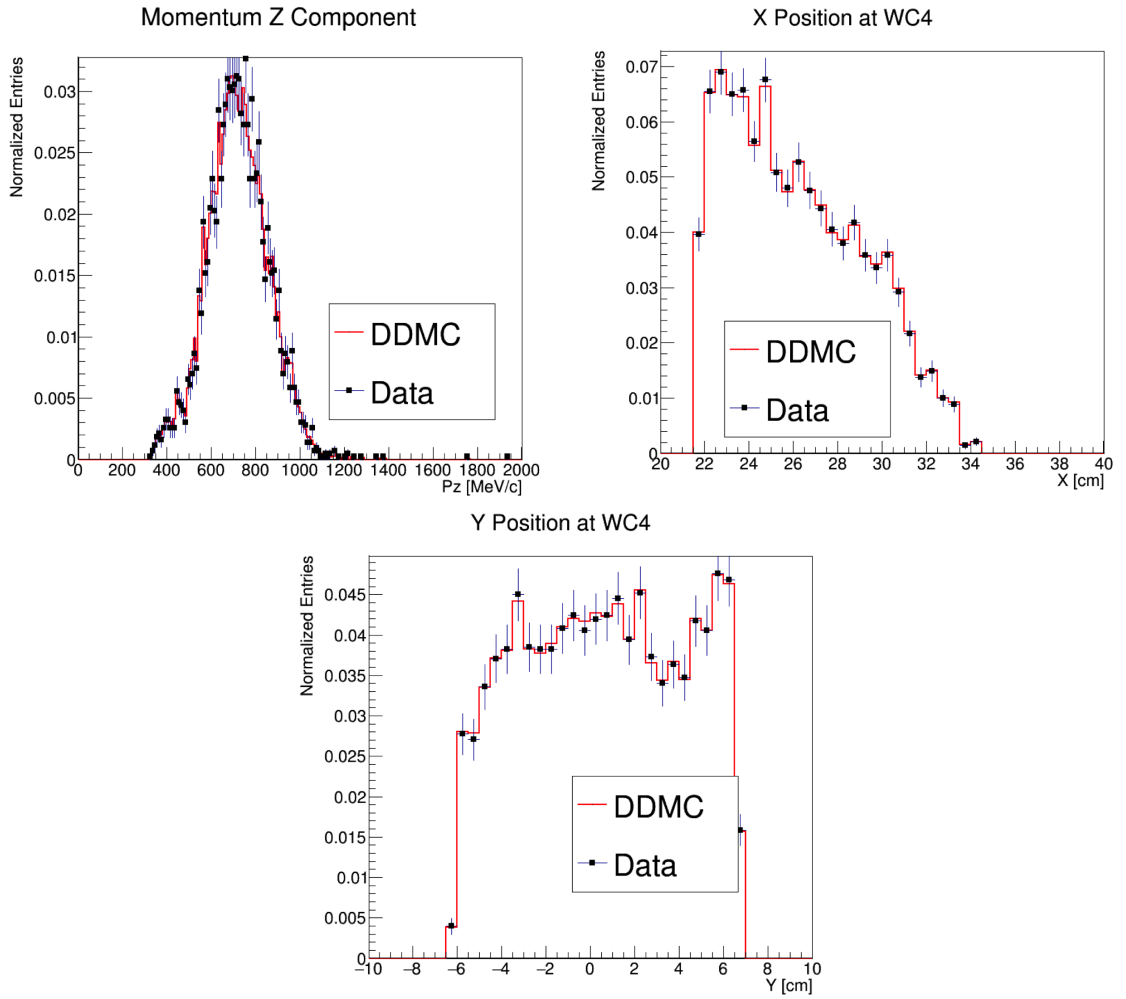


Figure 1.5: Comparison between generated quantities and data distributions for the 100A kaon sample: Z component of the momentum at WC4 (top left), X position at Wire Chamber 4 (top right), Y position at Wire Chamber 4 (bottom).

## 1.3 Estimate of Backgrounds in the Pion Cross Section

We use the beamline simulation and the DDMC simulation to estimate the background in the total hadronic pion cross section. Two categories of background exists for the negative pion cross section measurement: the one related to the pion interaction in the chamber, discussed in Section 1.3.1 and the one related to the beamline contamination, discussed in Section 1.3.2.

### 1.3.1 Background from Pion Capture and Decay

Our goal is to measure the total hadronic cross section for negative pions in argon. Since pion capture can be classified as an electromagnetic process and pion decay is a weak process, capture and decay represent unwanted interactions. We present here a study of capture and decay in Monte Carlo and the solution we adopted to mitigate their occurrence in the data sample.

For this MC study, we use a sample of MC pions generated according to the  $-60A$  beam profile with the DDMC (see Section 1.2.2). It is important to notice that capture occurs predominantly at rest, while decay may occur both in flight and at rest. Thus, we can highly mitigate capture and decay at rest by removing pions which would release all their energy in the TPC and stop. This translates into a momentum selection, where we keep only events whose WC momentum is above a certain threshold. Figure 1.6 shows the true momentum distribution for the primary pions<sup>1</sup> that arrive to the TPC (pink), that capture (green) or decay (blue) inside the TPC, on a linear scale (left) and on a log scale (right) vertical axis.

---

1. We use here the Geant4 denomination “primary” to indicate that the pion considered does not undergo interactions modifying its energy before getting to the TPC. In fact, not every pion shot from wire chamber four will arrive to the TPC as primary, some will decay or interact before the TPC.

470 In order to choose the selection value for the wire chamber momentum, it is  
 471 beneficial to estimate the ratio of events which capture or decay that survive the  
 472 selection in MC as a function of the momentum threshold, and compare it with the  
 473 survival ratio for all the 60A events. This is done in figure 1.7. We define the survival  
 474 ratio simply as the number of events surviving the true momentum selection divided  
 475 by the number of events of that category. We calculate the survival ratio separately  
 476 for the three event categories explained above: total (pink), capture (green) and decay  
 477 (blue). Selecting pions with momentum greater than 420 MeV/c reduces the capture  
 478 events by 99% while maintaining about 80% of the 60A data sample and almost  
 479 the entire 100A sample. Figure 1.8 shows the ratio of events which end their life in  
 480 capture (green) or decay (blue) over the total number of events as a function of  
 481 the true momentum at wire chamber four. This ratio is slightly dependent on the  
 482 inelastic cross section implemented in Geant4, as we are able to register a pion capture  
 483 (or decay) only if it did not interact inelastically in the TPC. We choose a momentum  
 484 threshold of 420 MeV/c because the percentage of capture events drops below 1% and  
 485 the percentage of decays is never above 2% for momenta greater than 420 MeV/c.  
 486 After the momentum selection, we evaluate the contribution of capture and decay to  
 487 be a negligibly small background to the cross section measurement compared to the  
 488 background related to the beamline which we will address in the next section.



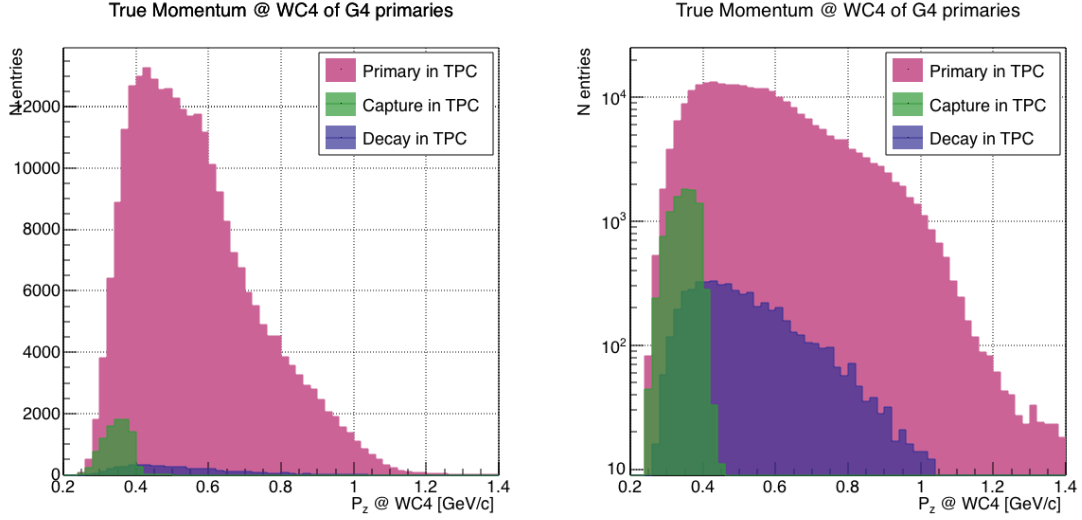


Figure 1.6: True momentum distribution at wire chamber 4 for every simulated pion arriving in the TPC (pink), ending its life in capture (green) or in decay (blue) in the TPC, linear vertical axis on the left, logarithmic on the right.

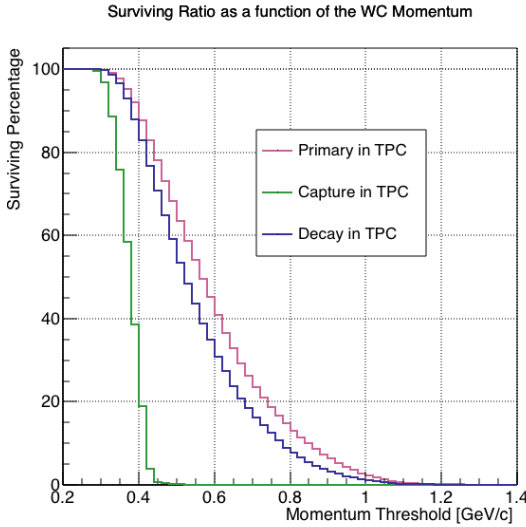


Figure 1.7: Survival ratio as a function of selection threshold on true momentum at wire chamber four for every simulated pion arriving in the TPC (pink), capture (green) or in decay (blue).

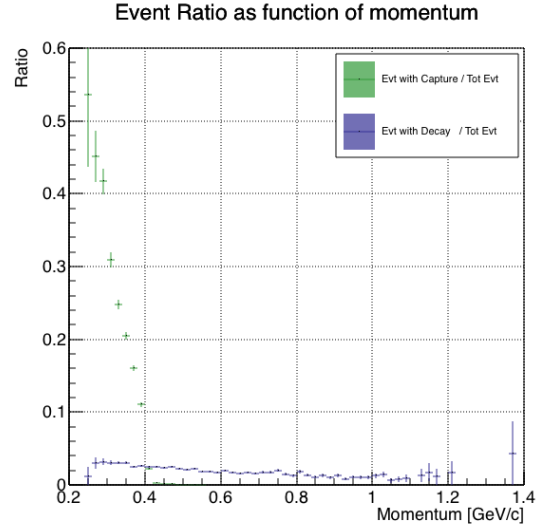


Figure 1.8: Ratio between the capture (green) and decay (blue) events over the total number of events as a function of the true momentum at wire chamber four.

### 1.3.2 Contributions from the Beamline Background

We define beamline background every TPC track matched to the WC track which is not a primary pion. Potentially, there are 4 different types of beamline background:

1) electrons,

2) muons,

3) secondaries from pion events,

4) matched pile up events.

The first step to quantify the effect of the beamline background on the pion cross section is to estimate what percentage of events used in the cross section calculation is not a primary pion. We start by noting that the last type of background, the “matched pile up” events, is a negligible fraction, because of the definition of the WC2TPC match: we deem the probability of a single match with a halo particle in the absence of a beamline particle<sup>2</sup> negligibly small. As shown in Section 1.2.1, we use G4Beamline to estimate the percentage of pions, muons and electrons at WC4, obtaining the composition shown in Table 1.2. The next step is to simulate those pions, muons and electrons from WC4 to the TPC with the DDMC and evaluate their contribution to the cross section. To do so, we start by simulating the same number of electrons, muons and pions with the DDMC and we apply the same selection chain (i.e. track multiplicity rejection, WC2TPC acceptance and shower rejection) on the three samples. The number of events per particle species surviving this selection is shown on table 1.3. In order to reproduce the closest make up of the beam to data, we weight each event of a given particle species according to the estimated beam composition. In case of 60A runs, for example, the weights are 0.688 for pions, 0.046 for muons and 0.266 for electrons.

---

2. Events with multiple WC2TPC matches are always rejected.

	Magnet Current -60A			Magnet Current -100 A		
	MC $\pi^-$	MC $\mu^-$	MC $e^-$	MC $\pi^-$	MC $\mu^-$	MC $e^-$
Total Initial events	334500	334500	334500	344500	344500	344500
After Multiplicity Rejection	330668	333420	198065	326576	344208	201380
After WC2TPC Selection	218239	296333	91139	230418	300228	98834
Evts After Shower Rejection	208063	288914	20293	219882	293585	17780
Selection Survival Rate	62.3%	86.6%	6.1%	63.8%	85.5%	5.2%
Beam Composition @WC4	68.8%	4.6 %	26.6 %	87.4 %	3.7 %	8.9 %
Beam Composition @TPC FF	88.5%	8.2%	3.3 %	94.0%	5.3%	0.7%

Table 1.3: MC selection flow per particle species.

513 It should be noted that pions may interact hadronically in the steel or in the  
 514 non-instrumented argon upstream to the TPC front face while travelling the length  
 515 of between WC4 and the TPC. Or, they could decay in flight between WC4 and the  
 516 TPC. One of the interaction products can leak into the TPC and be matched with the  
 517 WC track, contributing to the pool of events used for the cross section calculation. We  
 518 call this type of particles “secondaries” from pion events, with a terminology inspired  
 519 by Geant4. We estimate the number of secondaries using the DDMC pion sample.  
 520 The percentage of secondaries is given by the number of matched WC2TPC tracks  
 521 whose corresponding particle is not flagged as primary by Geant4. The secondary to  
 522 pion ratio is 4.9% in the 60A sample and 4.3% in the 100A sample.

523 We evaluate the beamline background contribution to the cross section by pro-  
 524 ducing the interacting and incident histograms for the events surviving the selection,  
 525 staggering the contributions for each particle species, as shown in Figure 1.9. From  
 526 those histograms, we are able to evaluate the contribution of pions and beamline  
 527 backgrounds to each bin of the interacting and incident histograms separately and  
 528 obtain the relative pion content. The relative pion content in each bin for the inter-  
 529 acting and incident histograms represents the correction applied to data. We take

530 here the interacting histogram as example, noting that the derivation of the correc-  
 531 tion for the incident histogram is identical. The number of entries in each bin of  
 532 the interacting plot (Figure 1.9 left) is  $N_{\text{Int}}^{\text{TOT}}(E_i)$ , equal to the sum of the pions and  
 533 beamline backgrounds in that bin, namely

$$N_{\text{Int}}^{\text{TOT}}(E_i) = N_{\text{Int}}^{\pi}(E_i) + \underbrace{N_{\text{Int}}^{\mu}(E_i) + N_{\text{Int}}^e(E_i) + N_{\text{Int}}^{\text{Secondary}}(E_i)}_{B_{\text{Int}}(E_i)}. \quad (1.1)$$

534 Thus, the relative pion content to each bin in MC can be calculated as follows

$$C_{\text{Int}}^{\pi MC}(E_i) = \frac{N_{\text{Int}}^{\pi MC}}{N_{\text{Int}}^{\text{TOTMC}}(E_i)} = \frac{N_{\text{Int}}^{\text{TOTMC}}(E_i) - B_{\text{Int}}^{\text{MC}}(E_i)}{N_{\text{Int}}^{\text{TOTMC}}(E_i)}. \quad (1.2)$$

535 In order to evaluate the pion content of each bin in data, we scale the measured  
 536 bin by the corresponding relative pion content found in MC, as follows

$$N_{\text{Int}}^{\pi \text{RecoData}} = N_{\text{Int}}^{\text{TOTData}}(E_i) - B_{\text{Int}}^{\text{Data}}(E_i) = C_{\text{Int}}^{\pi MC}(E_i) N_{\text{Int}}^{\text{TOTData}}(E_i). \quad (1.3)$$

537 The pion content is evaluated separately in the interacting and incident his-  
 538 tograms. Their ratio determines a correction to the measured raw cross section.  
 539 For example, the measured raw cross section of a sample with enhanced muons con-  
 540 tent will tend to be lower than the raw cross section of a muon free sample. This is  
 541 because most of the muons will cross the TPC without stopping, thus contributing  
 542 almost exclusively to the incident histogram, forcing the pion content to be lower  
 543 in the incident histogram than in the interacting; thus, the correction will tend to  
 544 enhance the cross section.

## 1.4 Estimate of Energy Loss before the TPC

The beamline particles travel a path from where their momentum is measured in the beamline until they are tracked again inside the TPC. In the LArIAT geometry, a particle leaving the WC4 will encounter the materials listed in Table 1.4 before being registered again. The energy lost by the particle in this non-instrumented material modifies the particle’s kinetic energy and directly affects the cross section measurement, as shown in equation 5.

Material	density [g/cm <sup>3</sup> ]	width [cm]
Fiberglass laminate (G10)	1.7	1.28
Liquid Argon	1.4	3.20
Stainless Steel	7.7	0.23
Titanium	4.5	0.04
Air	$1.2 \cdot 10^{-3}$	89.43
Plastic Scintillator	1.03	1.20 (+ 1.30)

Table 1.4: LArIAT material budget from WC4 to the TPC Front Face.

We derive an estimate of the energy loss between the beamline momentum measurement and the TPC ( $E_{loss}$ ) from the pion and kaon DDMC samples, since this quantity is not measurable directly on data. The  $E_{loss}$  distribution for the 60A and 100A pion sample is shown in figure 1.10, left and right respectively. The  $E_{loss}$  distribution for the whole kaon sample is shown in figure 1.11. A clear double peaked structure is visible, which is due to the particles either missing or hitting the HALO paddle: a schematic rendering of this occurrence is shown in figure 1.12. The kinematic at WC4 determines the trajectory of a particle and whether or not it will hit the halo paddle. In figure 1.13, we plot the true horizontal component of the momentum  $P_x$  versus the true  $X$  position at WC4 for pions missing the halo paddle (left) and for pions hitting the halo paddle (right) for the -60A MC simulation runs – analogous plots are obtained with the -100A pion simulation and with the kaon simulation. These distributions can be separated drawing a line in this position-momentum space.

We use a logistic regression [13] as a classifier to find the best separating line, shown in both plots as the red line. We classify as “hitting the halo paddle” all pions whose  $P_x$  and  $X$  are such that

$$P_x + 0.02 * X - 0.4 < 0$$

and as “missing the halo paddle” all pions whose  $P_x$  and  $X$  are such that

$$P_x + 0.02 * X - 0.4 > 0,$$

where the coefficients of the line are empirically found by the logistic regression estimation. Overall, this simple method classifies in the right category (hit or miss) about 86% of the pion events. In MC, we assign  $E_{loss} = 32 \pm 4$  MeV for pion events classified as “hitting the halo paddle”; we assign  $E_{loss} = 24 \pm 3$  MeV for pion events classified as “missing the halo paddle”. We apply the same classifier on data.

A scan of the simulated geometry showed an excess of 3 cm of uninstrumented argon compared with the surveyed detector geometry. We account for this difference by assigning in data  $E_{loss} = 24 \pm 6$  MeV for pion events classified as “hitting the halo paddle” and  $E_{loss} = 17 \pm 6$  MeV for pion events classified as “missing the halo paddle”, where the uncertainty is derived as the standard deviation of the double peaked distribution.

The summary of the values for used for  $E_{Loss}$  for the pion sample is listed in table 1.5 with the analogous results for the study on the kaon case.

	$E_{loss}$ [MeV]	
	Hitting Halo	Missing Halo
Pion MC	$32 \pm 4$	$24 \pm 3$
Pion Data	$25 \pm 6$	$17 \pm 6$
Kaon MC	$38 \pm 6$	$31 \pm 5$
Kaon Data	$26 \pm 7$	$22 \pm 7$

Table 1.5: Energy loss for pions and kaons.

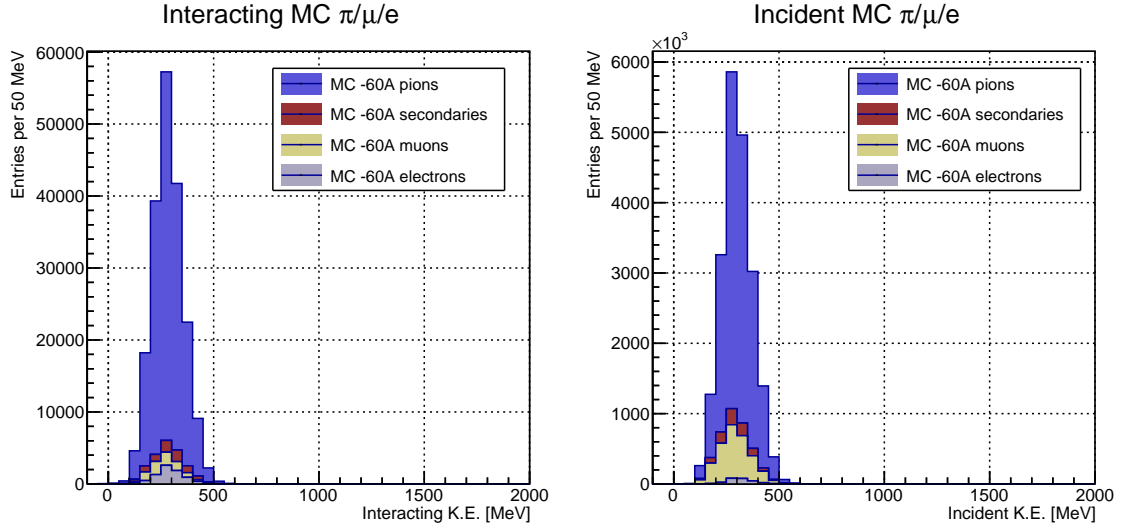


Figure 1.9: Left: staggered contributions to the interacting kinetic energy distribution for electron (grey), muons (yellow) and pion (blue) in the 60A simulation sample. Right: staggered contributions to the incident kinetic energy distribution for electron (grey), muons (yellow) and pion (blue) in the 60A simulation sample.

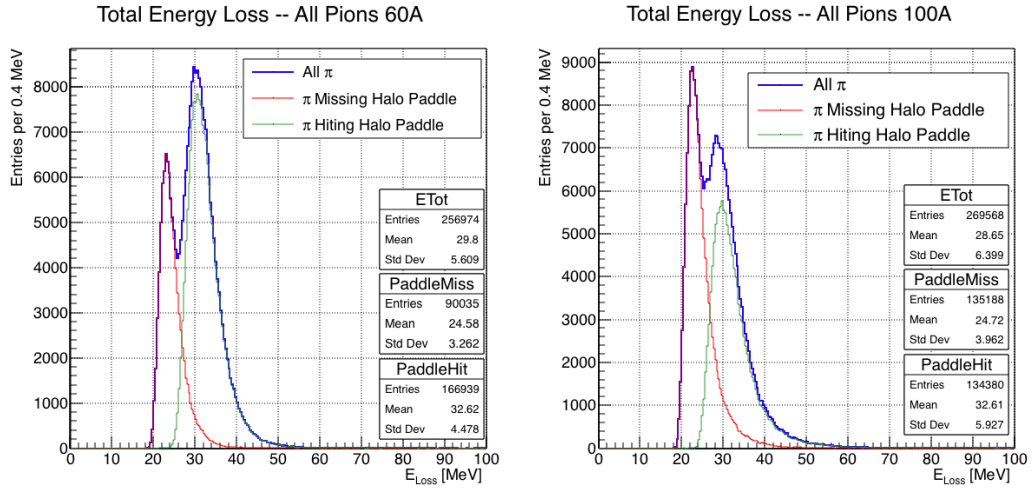


Figure 1.10: True energy loss between WC4 and the TPC front face according to the MC simulation of negative pions of the 60A runs (left) and of the 100A runs (right). The distribution for the whole data sample is shown in blue, the distribution for the pions missing the halo is shown in red, and the distribution for the pions hitting the halo is shown in green.

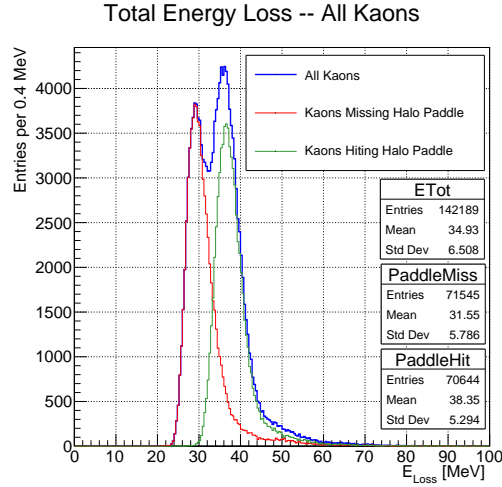


Figure 1.11: True energy loss between WC4 and the TPC front face according to the MC simulation of positive kaons in the 60A and 100A combined sample. The distribution for the whole data sample is shown in blue, the distribution for the kaons missing the halo is shown in red, and the distribution for the kaons hitting the halo is shown in green.

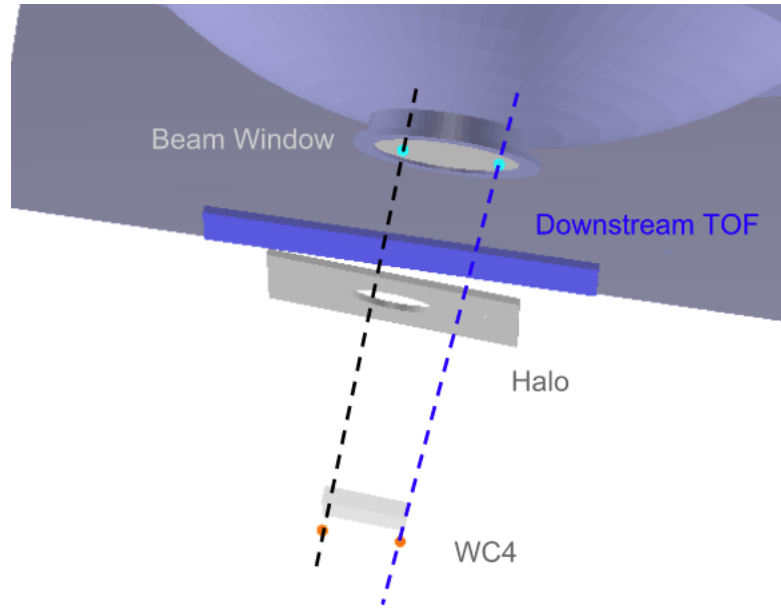


Figure 1.12: Schematic rendering of the particle path between WC4 and the TPC front face. The paddle with the hollow central circle represents the Halo paddle. We illustrate two possible trajectories: in black, a trajectory that miss the paddle and goes through the hole in the Halo, in blue a trajectory that hits the Halo paddle and goes through the scintillation material.



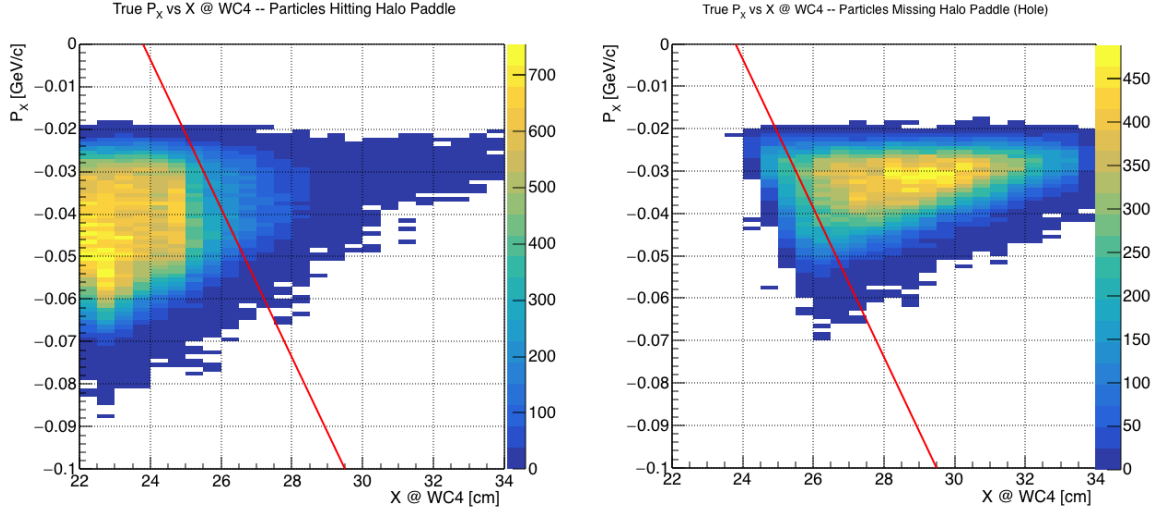


Figure 1.13: Horizontal component of the true momentum vs the horizontal position at WC4 for MC simulated pions of the 60A runs. The plot on the left shows the distribution for pion that miss the halo paddle and the plot on the right shows the distributions for pions that hit the halo. The form of the classifier is overlaid to both plots (red line).

## 1.5 Tracking Studies

The tracking of hadrons in the TPC determines both the beamline to TPC handshake and the identification of the interaction point within the TPC. Thus, it plays a fundamental role in the cross section measurements. We performed several studies geared towards the optimization of the package for tracking in the TPC. In particular, we studied a suitable set of parameters for the WC2TPC match and we optimized the clustering algorithm to maximize the efficiency of finding the interaction point on MC. Given the technical nature of these studies, we report them in Appendix A. We report here the evaluation of the angular resolution of the tracking algorithm in data and MC, due to its implication on the physics measurement.

### 1.5.1 Angular Resolution

Scope of this study is to understand and compare the tracking performances and angular resolution of the TPC tracking on data and MC. We use the angular resolution

of the tracking to determine the value of smallest angle that we can reconstruct with a non-zero efficiency, effectively determining a selection on the angular distribution of the cross section measurement due to the tracking performance.

We start by selecting all the WC2TPC matched tracks used for the cross section analysis. These tracks can contain from a minimum of 3 3D-space points to a maximum of 240 3D-space points. We fit a line to all the 3D-space points associated with the track. For each track we calculate the average distance between each point in space and the fit line as follows

$$\bar{d} = \frac{\sum_i^N d_i}{N}, \quad (1.4)$$

where  $N$  is the number of 3D-space points of the track and  $d_i$  is the distance of the  $i$ -th space point to the line fit. Several tests to compare the goodness of fit between data and MC have been considered. We decided to use  $\bar{d}$  for its straightforward interpretation. The  $\bar{d}$  distribution for data and MC is shown in Figure 1.16 for pions and in Figure 1.18 for kaons and shows a relatively good agreement between data and MC.

A visual representation of the procedure used to evaluate the angular resolution is shown in Figure 1.14. For each track, we order the space points according to their Z position along the positive beam direction (panel a) and we split them in two sets: the first set contains all the points belonging to the first half of the track and the second set contains all the points belonging the second half of the track. We remove the last four points in the first set and the first four points in the second set, so to have a gap in the middle of the original track (panel b). We fit the first and the second set of points with two lines (panel c). We then calculate the angle between the fit of the first and second half  $\alpha$  (panel d). The angle  $\alpha$  determines the spatial resolution of the tracking. The distributions for data and MC for  $\alpha$  are given in Figure 1.17 for pions and in Figure 1.19 for kaons. The mean of the data and MC angular resolution are reported in Table tab:AngRes for pions and kaons in data and MC.

Interaction angles smaller than the angle resolution are indistinguishable for the reconstruction. Therefore, we assess our ability to measure the cross section to be limited to interaction angles greater than 5.0 deg. More accurate studies of the angular resolution as a function of the kinetic energy and track length, albeit interesting, are left for an improvement of the analysis.

It is beneficial to take a moment to describe the definition of interaction angle. In case of elastic scattering, the definition is straightforward: the interaction angle is the angle between the incoming and outgoing hadron, i.e.

$$\theta = \cos^{-1} \left( \frac{\vec{p}_{\text{incoming}} \cdot \vec{p}_{\text{outgoing}}}{|\vec{p}_{\text{incoming}}| |\vec{p}_{\text{outgoing}}|} \right). \quad (1.5)$$

In case of inelastic scattering, the presence of several topologies requires a more complex definition, as shown in figure 1.15. We define the scattering angle as the biggest of the angles between the incoming hadron and the visible daughters, where the visible daughters are charged particles that travel more than 0.47 cm in the detector (see panel a); in case all the daughters are invisible, the angle is assigned to be 90 deg (see panel b). We chose this working definition of scattering angle for inelastic scattering keeping in mind how our tracking reconstruction works: the tracking will stop correctly non of the daughters are is visible in the detector and it is likely to stop correctly if multiple daughters form an interaction vertex. The only “dangerous” case is the production of one charged daughter plus neutrals, which we can study with this working definition of scattering angle (see panel c).

We can see the effects of the angular resolution on the cross section by plotting the true Geant4 cross section for interaction angles greater than a minimum interaction

	Data	MC
Pions	$\bar{\alpha}_{Data} = (5.0 \pm 4.5) \text{ deg}$	$\bar{\alpha}_{MC} = (4.5 \pm 3.9) \text{ deg}$
Kaons	$\bar{\alpha}_{Data} = (4.3 \pm 3.7) \text{ deg}$	$\bar{\alpha}_{MC} = (4.4 \pm 3.6) \text{ deg}$

Table 1.6: Angular resolution for Pion and Kaon tracking in both data and MC.

angle. Figure 1.20 shows the true Geant4 cross section for interaction angles greater  
 than 0 deg (green), 4.5 deg (red), 5.0 deg (blue) and 9.0 deg (yellow). A small 0.5 deg  
 systematic shift between the mean of the data and MC angular resolution is present.

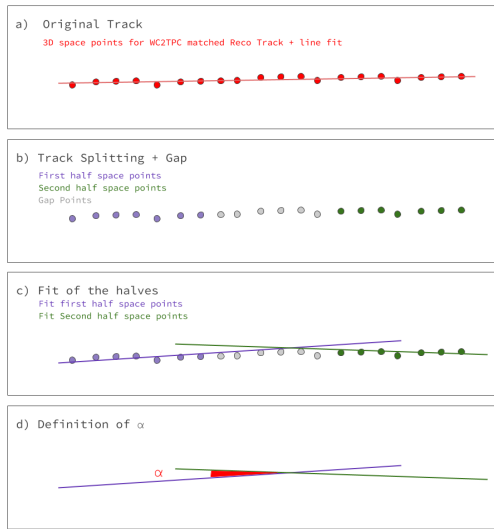


Figure 1.14: A visual representation of the procedure used to evaluate the angular resolution.

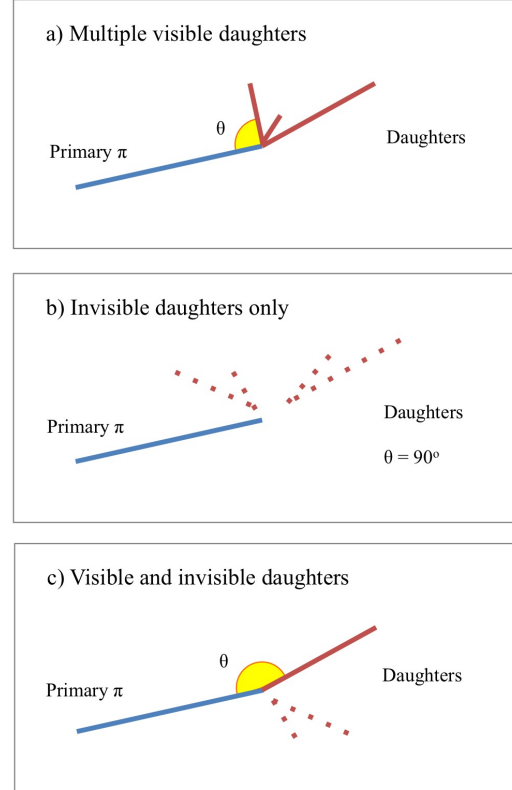


Figure 1.15: A visual representation of the scattering angle definition in case of inelastic scattering.

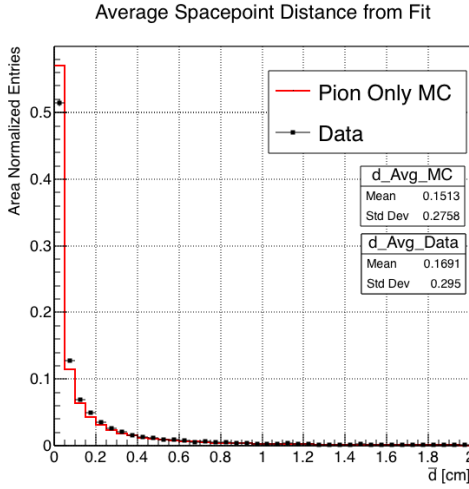


Figure 1.16: Distributions of the average distance between each 3D point in space and the fit line,  $\bar{d}$  for the data used in the pion cross section analysis and the pion only DDMC. The distributions are area normalized.

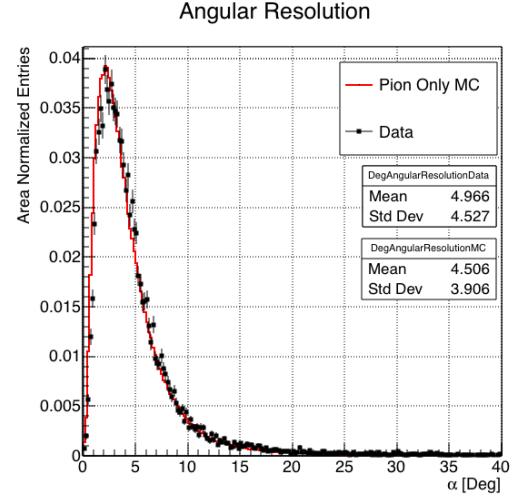


Figure 1.17: Distributions of angular resolution  $\alpha$  for data used in the pion cross section analysis and pion only DDMC. The distributions are area normalized.

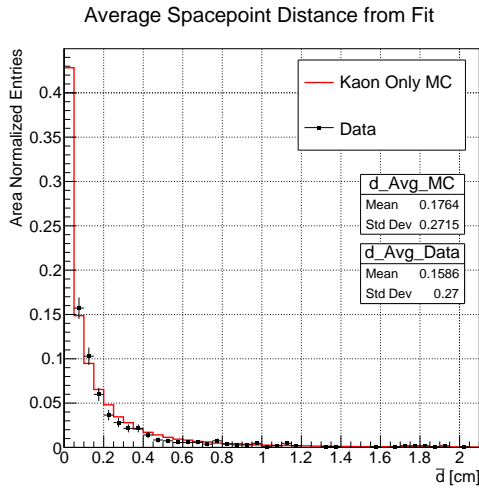


Figure 1.18: Distributions of the average distance between each 3D point in space and the fit line,  $\bar{d}$  for the data used in the kaon cross section analysis and the kaon only DDMC. The distributions are area normalized.

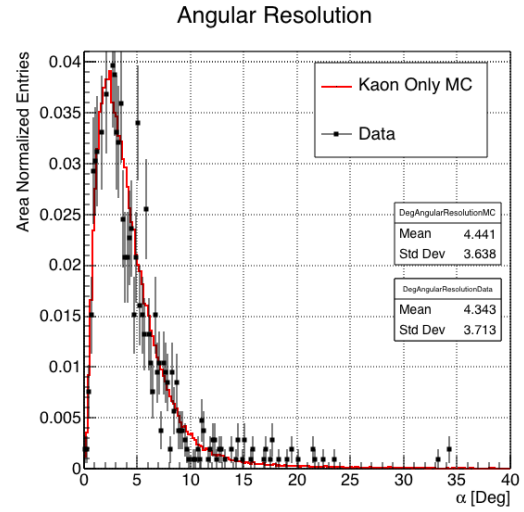


Figure 1.19: Distributions of angular resolution  $\alpha$  for data used in the kaon cross section analysis and kaon only DDMC. The distributions are area normalized.

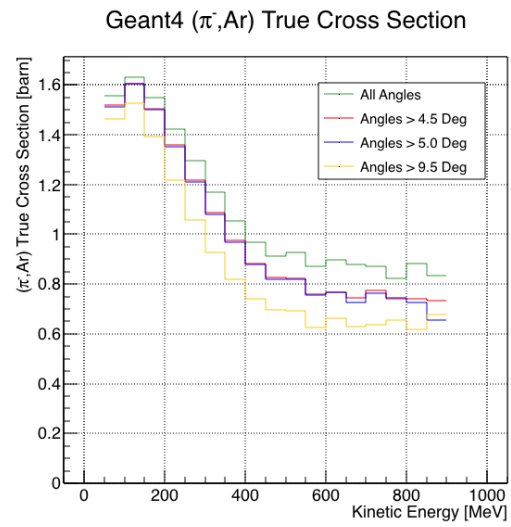


Figure 1.20: True ( $\pi^-$ , Ar) cross section for interaction angles greater than 0 deg (green), 4.5 deg (red), 5.0 deg (blue) and 9.0 deg (yellow).

## 1.6 Calorimetry Studies

The measured kinetic energy of a hadron candidate at each argon slab determines which bins of the interacting and incident histograms a selected event is going to fill. Thus, the energy measurement provided by the LArTPC is fundamental for the cross section analysis. In Appendix B, we describe how we calibrate the TPC calorimetric response. In the following section, we describe how we measure the kinetic energy of the hadrons in the TPC.

### 1.6.1 Kinetic Energy Measurement

In this section, we define the measurement on the kinetic energy and determine the related uncertainty. We will propagate this uncertainty into the cross section measurement, as discussed in Section 2.1.2 for the pion cross section and in Section ?? for the kaon cross section.

The kinetic energy of a hadron at the  $j^{\text{th}}$  slice of argon in the TPC is given by

$$KE_j = \sqrt{p_{Beam}^2 + m_{Beam}^2} - m_{Beam} - E_{Loss} - E_{FF-j}, \quad (1.6)$$

where  $p_{Beam}$  is the momentum measured by the beamline detectors,  $m_{Beam}$  is the mass of the hadron as reported in the PDG,  $E_{Loss}$  is the energy loss between the beamline and the TPC, and  $E_{FF-j}$  is the energy that the hadron deposited from the TPC front face until the  $j^{\text{th}}$  slice. The uncertainty on  $KE_j$  is then given by

$$\delta KE_j = \sqrt{\delta p_{Beam}^2 + \delta E_{Loss}^2 + \delta E_{dep\ FF-j}^2}, \quad (1.7)$$

where we have dropped the uncertainty on the mass, since it is orders of magnitude smaller than the other uncertainties. We assume the relative uncertainty on  $p_{Beam}$  to be 2%, and the uncertainty on the energy loss upstream to be 7 MeV, as calculated

648 in Section 1.4. We describe the estimate of the uncertainty on  $E_{\text{FF-j}}$  in the rest of  
 649 this section.

650 The energy deposited by the hadron from the TPC front face until the  $j^{\text{th}}$  slice is  
 651 the sum of the measured energy deposited in each previous slabs  $E_i$ , i.e.

$$E_{\text{FF-j}} = \sum_{i < j} E_i, \quad (1.8)$$

652 where  $E_i$  is measured in each slab as the product of the stopping power,  $dE/dX_i$ ,  
 653 and the track pitch,  $Pitch_i$ , for that point. If we assume conservatively that the  
 654 measurements of  $E_i$  are not independent from one another, the uncertainty on  $E_{\text{FF-j}}$   
 655 becomes

$$\delta E_{\text{FF-j}} = (j - 1)\delta E_i, \quad (1.9)$$

656 where  $\delta E_i$  is the uncertainty on the energy loss in one slab of argon.

657 The left side of Figure 1.21 shows the distribution of the energy deposited in each  
 658 slab of argon, for the 60A negative pion dataset in black and for the pion only MC  
 659 in blue. The analogous plot for the -100A negative pion data set is show on the right  
 660 side of Figure 1.21. The distributions are fitted with a landau displayed in red for  
 661 data and in teal for MC. The uncertainty on  $E_i$  is given by the width of the Landau  
 662 fit to the data. A small systematic uncertainty is given by a 1.0% difference between  
 663 the most probable value of the landau fits in data and MC.



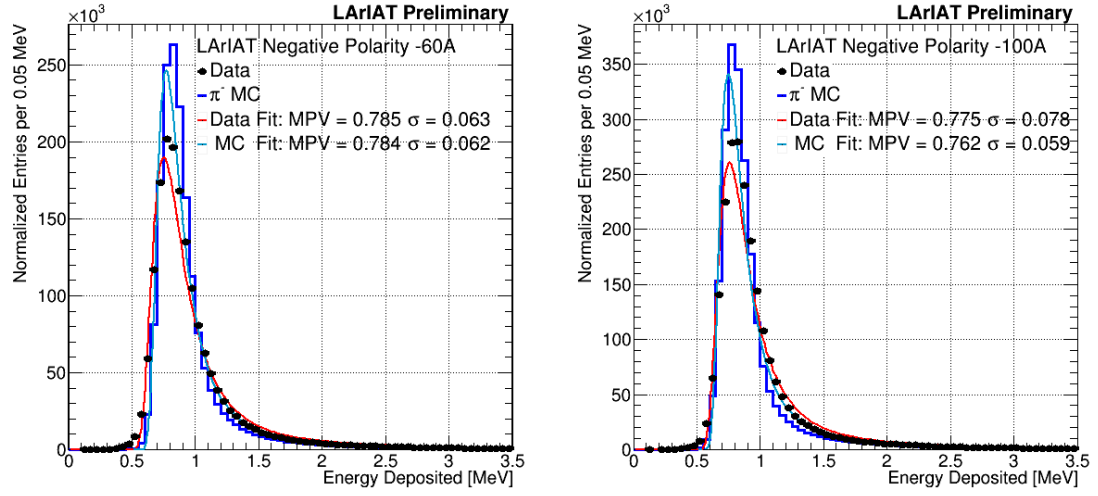


Figure 1.21: Energy deposited  $E_i$  in a single slab of argon for the pion -60A runs (left) and -100A runs (right). The data is shown in black, the MC in blue. The distributions are fitted with a landau displayed in red for data and in teal for MC.

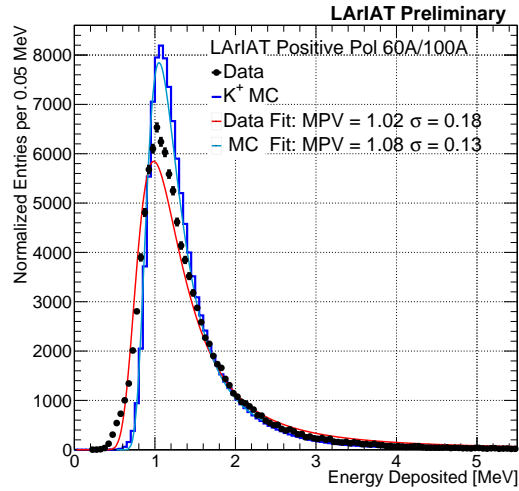


Figure 1.22: Energy deposited  $E_i$  in a single slab of argon for the kaons of the +60A runs and +100A runs. The data is shown in black, the MC in blue. The distributions are fitted with a landau displayed in red for data and in teal for MC.

## Chapter 2

# Negative Pion Cross Section Measurement

*“Y ella es flama que se eleva, Y es un pájaro a volar.  
En la noche que se incendia, estrella de oscuridad  
que busca entre la tiniebla, la dulce hoguera del beso.”*  
– Lila Downs, Benediction And Dream, 2002 –

In this chapter, we show the result of the thin slice method to measure the ( $\pi^-$ -Ar) total hadronic cross section. In Section 2.1, we start by measuring the raw cross section, i.e. the cross section obtained exclusively using data reconstruction, without any additional corrections. In Section 2.2, we apply a statistical subtraction of the background contributions based on simulation and a correction for detection inefficiency. The final results are presented in Section 2.3.

### 2.1 Raw Cross Section

We measure the raw ( $\pi^-$ -Ar) total hadronic cross section as a function of the kinetic energy in the two chosen data sets, the -60A and -100A negative runs. As we will

clarify in Section 2.2, the corrections to the raw cross section depend on the beam conditions and need to be calculated independently for the two datasets. Thus, we present here the measurement of the raw cross section on the two datasets separately.

As stated in section 0.3.2, the raw cross section is given by the equation 4

$$\sigma_{TOT}(E_i) = \frac{1}{n\delta X} \frac{N_{Int}^{TOT}(E_i)}{N_{Inc}^{TOT}(E_i)}, \quad (2.1)$$

where  $N_{Int}^{TOT}$  is the measured number of particles interacting at kinetic energy  $E_i$ ,  $N_{Inc}^{TOT}$  is the measured number of particles incident on an argon slice at kinetic energy  $E_i$ ,  $n$  is the density of the target centers and  $\delta X$  is the thickness of the argon slice. The density of the target centers and the slab thickness are  $n = 0.021 \cdot 10^{24} \text{ cm}^{-3}$  and  $\delta X = 0.47 \text{ cm}$ , respectively.

Figure 2.1 shows the distribution of  $N_{Int}^{TOT}$  as a function of the kinetic energy for the 60A dataset on the left and for the 100A dataset on the right. The data central points are represented by black dots, the statistical uncertainty is shown in black, while the systematic uncertainty is shown in red. Data is displayed over the  $N_{Int}^{TOT}$  distribution obtained with a MC mixed sample of pions, muon and electrons (additional details on the composition will be provided in Section ??). The contribution from the simulated pions is shown in blue, the one from secondaries in red, the one from muons in yellow and the ones from electrons in gray. The simulated pion's and backgrounds' contributions are stacked; the sum of the integrals from each particle species is normalized to the integral of the data.

Figure 2.2 shows the distribution of  $N_{Inc}^{TOT}$  for the 60A dataset on the left and for the 100A dataset on the right. Data is displayed over the MC. The same color scheme and normalization procedure is used for both the interacting and incident histograms.

Figure 3.3 shows the raw cross section for the 60A dataset on the left and for the 100A dataset on the right, statistical uncertainty in black and systematic uncertainty

in red. The raw data cross section is overlaid to the reconstructed cross section for the MC mixed sample, displayed in azure. Since the background contributions and the detector effects for the 60A and 100A sample are different, it is premature to compare the raw cross sections obtained from the two samples at this point.

We describe the calculation of the statistical uncertainty for the interacting, incident and cross section distributions in Section 2.1.1; we describe the procedure to calculate the corresponding systematics uncertainty on Section 2.1.2.

### 2.1.1 Statistical Uncertainty

The statistical uncertainty for a given kinetic energy bin of the cross section is calculated by error propagation from the statistical uncertainty on  $N_{\text{Inc}}^{\text{TOT}}$  and  $N_{\text{Int}}^{\text{TOT}}$  correspondent bin. Since the number of incident particles in each energy bin is given by a simple counting, we assume that  $N_{\text{Inc}}^{\text{TOT}}$  is distributed as a poissonian with mean and variance equal to  $N_{\text{Inc}}^{\text{TOT}}$  in each bin. On the other hand,  $N_{\text{Int}}^{\text{TOT}}$  follows a binomial distribution: a particle in a given energy bin might or might not interact. The variance for the binomial is given by

$$\text{Var}[N_{\text{Int}}^{\text{TOT}}] = \mathcal{N} P_{\text{Interacting}} (1 - P_{\text{Interacting}}). \quad (2.2)$$

Since the interaction probability  $P_{\text{Interacting}}$  is  $\frac{N_{\text{Int}}^{\text{TOT}}}{N_{\text{Inc}}^{\text{TOT}}}$  and the number of tries  $\mathcal{N}$  is  $N_{\text{Inc}}^{\text{TOT}}$ , equation 2.2 translates into

$$\text{Var}[N_{\text{Int}}^{\text{TOT}}] = N_{\text{Inc}}^{\text{TOT}} \frac{N_{\text{Int}}^{\text{TOT}}}{N_{\text{Inc}}^{\text{TOT}}} (1 - \frac{N_{\text{Int}}^{\text{TOT}}}{N_{\text{Inc}}^{\text{TOT}}}) = N_{\text{Int}}^{\text{TOT}} (1 - \frac{N_{\text{Int}}^{\text{TOT}}}{N_{\text{Inc}}^{\text{TOT}}}). \quad (2.3)$$

$N_{\text{Inc}}^{\text{TOT}}$  and  $N_{\text{Int}}^{\text{TOT}}$  are not independent. The statistical uncertainty on the cross section is thus calculated as

$$\delta\sigma_{\text{TOT}}(E) = \sigma_{\text{TOT}}(E) \left( \frac{\delta N_{\text{Int}}^{\text{TOT}}}{N_{\text{Int}}^{\text{TOT}}} + \frac{\delta N_{\text{Inc}}^{\text{TOT}}}{N_{\text{Inc}}^{\text{TOT}}} \right) \quad (2.4)$$

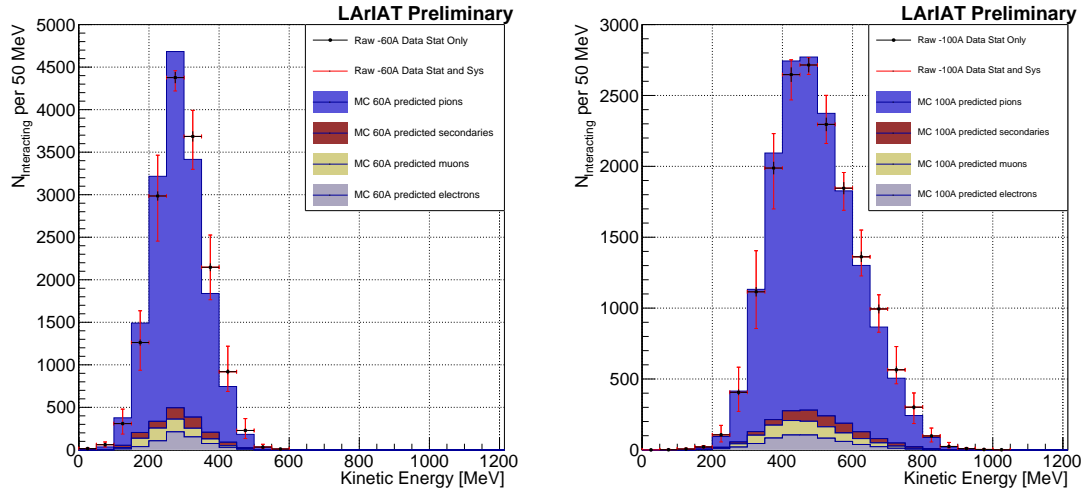


Figure 2.1: Raw number of interacting pion candidates as a function of the reconstructed kinetic energy for the 60A runs (left) and for the 100A runs (right). The statistical uncertainties are shown in black, the systematic uncertainties in red.

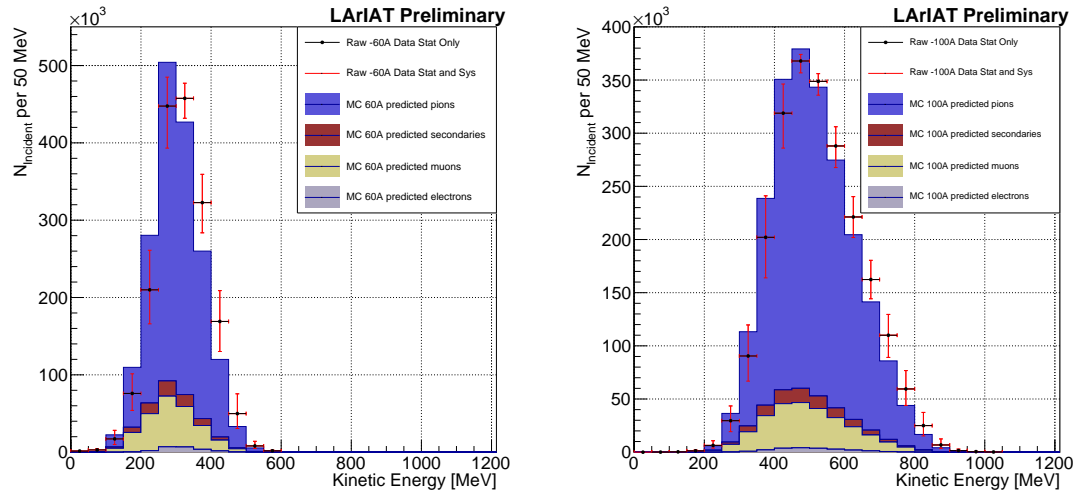


Figure 2.2: Raw number of incident pion candidates as a function of the reconstructed kinetic energy for the 60A runs (left) and for the 100A runs (right). The statistical uncertainty is shown in black, the systematic uncertainties in red.

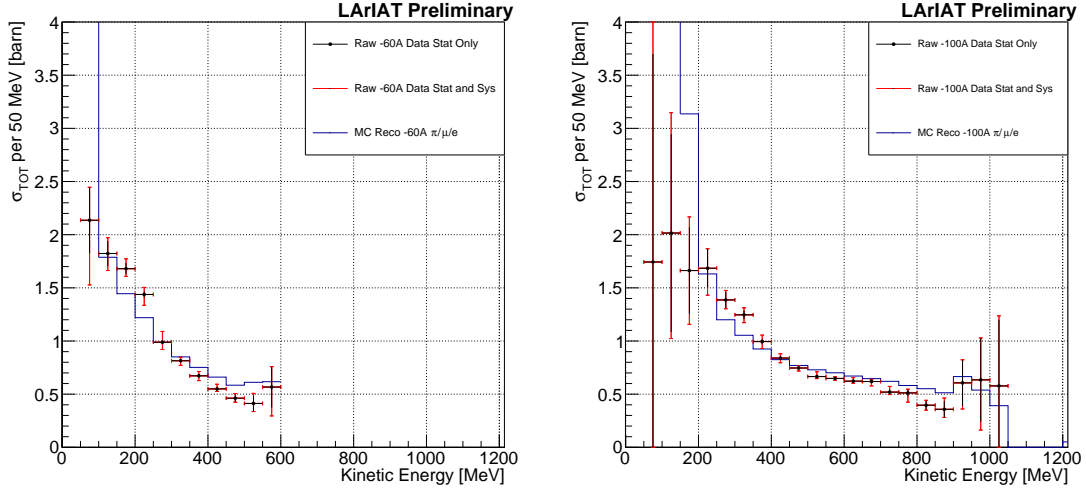


Figure 2.3: Raw ( $\pi^-$ -Ar) total hadronic cross section for the 60A runs (left) and for the 100A runs (right). The statistical uncertainty is shown in black, the systematic uncertainties in red. The raw cross section obtained with a MC mixed sample of pions, muon and electrons in the percentage predicted by G4Beamline is shown in azure.

723 where:

$$\delta N_{\text{Inc}}^{\text{TOT}} = \sqrt{N_{\text{Inc}}^{\text{TOT}}} \quad (2.5)$$

$$\delta N_{\text{Int}}^{\text{TOT}} = \sqrt{N_{\text{Int}}^{\text{TOT}} \left( 1 - \frac{N_{\text{Int}}^{\text{TOT}}}{N_{\text{Inc}}^{\text{TOT}}} \right)}. \quad (2.6)$$

## 724 2.1.2 Treatment of Systematics

725 The only systematic effect considered in the measurement of the raw cross section  
 726 results from the propagation of the uncertainty associate with the measurement of  
 727 the kinetic energy at each argon slab. As shown in Section 1.6.1, the uncertainty on  
 728 the kinetic energy of a pion candidate at the  $j^{\text{th}}$  slab of argon is given by

$$\delta KE_j = \sqrt{\delta p_{\text{Beam}}^2 + \delta E_{\text{Loss}}^2 + \delta E_{\text{dep FF-j}}^2} \quad (2.7)$$

$$= \sqrt{(2\% p_{\text{Beam}})^2 + (6 \text{ [MeV]})^2 + (j-1)^2 (\sim 0.08 \text{ [MeV]})^2}. \quad (2.8)$$

729 We propagate this uncertainty by varying the energy measurement  $KE_j$  at each  
 730 argon slab. We measure  $N_{\text{Inc}}^{\text{TOT}}$ ,  $N_{\text{Int}}^{\text{TOT}}$  and the cross section in three cases: first  
 731 assigning the measured  $KE_j$  at each kinetic energy sampling, then assigning  $KE_j +$   
 732  $\delta KE_j$ , and finally assigning  $KE_j - \delta KE_j$ . The difference between the values obtained  
 733 using the  $KE_j$  sampling and the maximum and minimum values in each kinetic energy  
 734 bin determines the systematic uncertainty.

## 735 2.2 Corrections to the Raw Cross Section

736 As described in section 0.3.3, we need to apply a background correction and an  
 737 efficiency correction in order to derive the true pion cross section from the raw cross  
 738 section. The true cross section is given in equation 9,

$$\sigma_{TOT}^{\pi^-}(E_i) = \frac{1}{n\delta X} \frac{\epsilon^{\text{Inc}}(E_i)}{\epsilon^{\text{Int}}(E_i)} \frac{C_{\text{Int}}^{\pi MC}(E_i)}{C_{\text{Inc}}^{\pi MC}(E_i)} \frac{N_{\text{Int}}^{\text{TOT}}(E_i)}{N_{\text{Inc}}^{\text{TOT}}(E_i)}. \quad (9)$$

739 Section 2.2.1 describes the evaluation of pion content in the interacting and inci-  
 740 dent histograms, ( $C_{\text{Int}}^{\pi MC}(E_i)$  and  $C_{\text{Inc}}^{\pi MC}(E_i)$ ) and the propagation to the cross section  
 741 measurement of the relative systematic uncertainties.

742 Section 2.2.2 describes the procedure employed to obtain the efficiency corrections  
 743  $\epsilon^{\text{Int}}(E_i)$  and  $\epsilon^{\text{Inc}}(E_i)$  and the propagation to the cross section measurement of the  
 744 relative uncertainties.

### 745 2.2.1 Background subtraction

746 We use the procedure described in 1.3.2 to evaluate the relative pion content in  
 747 the interacting histogram  $C_{\text{Int}}^{\pi MC}(E_i)$  and the relative pion content in the incident  
 748  $C_{\text{Inc}}^{\pi MC}(E_i)$ . We start by evaluating the relative pion content assuming the beamline  
 749 composition simulated by G4Beamline, whose pion, muon and electron percentages  
 750 per beam condition are reported again in the first line of Table 2.1. The left side of

751 Figure 2.4 shows the MC estimated relative pion content for the interacting histogram  
 752 as function of kinetic energy for the 60A runs (top) and 100A runs (bottom). The  
 753 right side of the same figure shows the MC estimated relative pion content for the  
 754 incident histogram as function of kinetic energy for the 60A runs (top) and 100A  
 755 runs (bottom). In Figure 2.4 the central curves displayed in light blue are obtained  
 756 using the beamline composition as predicted by G4Beamline: these are the correction  
 757 curves for the relative pion content applied to data.

758 So, the question now becomes: how well do we know the beamline composition?  
 759 In absence of additional data constraints, we take a 100% systematic uncertainty on  
 760 the electron content, reported in lines 3 and 4 of Table 2.1. The effect of doubling or  
 761 halving the electron percentage in the beam on the pion relative content is displayed  
 762 in red in Figure 2.4. We reserve a slightly different treatment for the muon content.  
 763 Since G4Beamline tracks only particles which cross all the wire chambers, pion events  
 764 that decay in flight from WC1 to WC4 are not recorded by G4Beamline. Pion decays  
 765 in the beamline could be trigger the beamline detectors in data, if the produced muon  
 766 proceeds in the beamline. Thus, we take the G4Beamline prediction for muons as a  
 767 lower bound in the composition: the effect of doubling the muon content (line 2 in  
 768 Table 2.1) is shown in blue on Figure 2.4. A future study of data from additional  
 769 beamline detectors such as the Aerogel Chernkov detectors [42] or the muon range  
 770 stack (see Section ??) has the potential of a narrowing the systematics uncertainty  
 771 coming from the beamline composition.

772 We propagate the uncertainty on the beamline composition as a systematic un-  
 773 certainty to the cross section by varying the beam composition for all the cases listed  
 774 in Table 2.1 and evaluating variation of obtained data cross sections in each bin. This  
 775 systematic uncertainty is summed in quadrature with the statistical uncertainty and  
 776 the systematic uncertainty related to the kinetic energy measurement.



	Magnet Current -60A			Magnet Current -100 A		
	MC $\pi^-$	MC $\mu^-$	MC $e^-$	MC $\pi^-$	MC $\mu^-$	MC $e^-$
Expected Composition	68.8 %	4.6 %	26.6 %	87.4 %	3.7 %	8.9 %
Composition 2x Muons	64.2 %	9.2 %	26.6 %	83.7 %	7.4 %	8.9 %
Composition 2x Electrons	42.2 %	4.6 %	53.2 %	78.5 %	3.7 %	17.8 %
Composition 0.5x Electrons	82.1 %	4.6 %	13.3 %	91.9 %	3.7 %	4.4 %

Table 2.1: Beam composition variation for the study of systematics due to beam contamination.

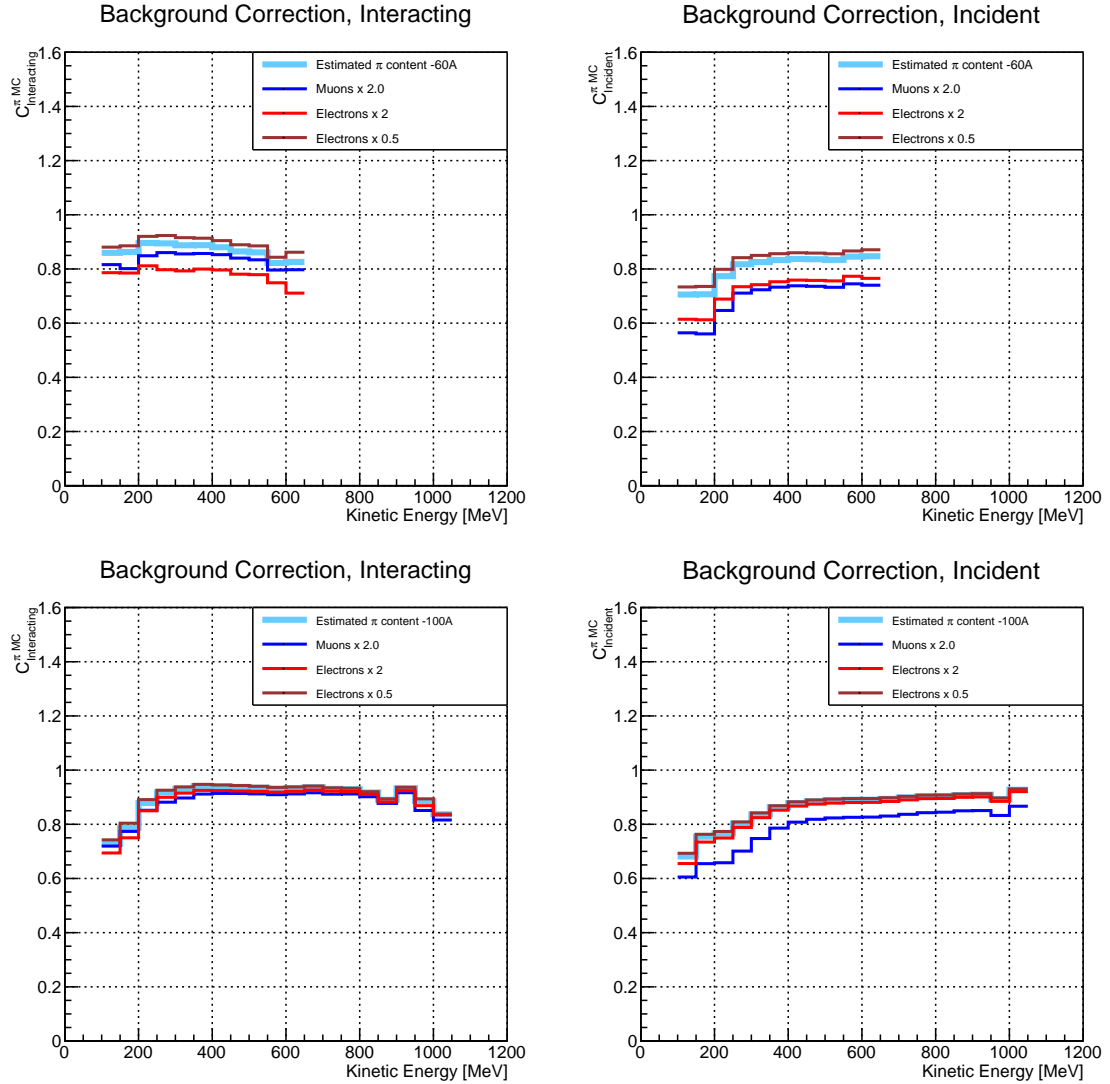


Figure 2.4: *Left:* MC estimated relative pion content for interacting histogram a function of kinetic energy for the 60A runs (top) and 100A runs (bottom), statistics uncertainty in azure and systematic uncertainty in blue. *Right:* MC estimated relative pion content for incident histogram a function of kinetic energy for the 60A runs (top) and 100A (bottom), statistics uncertainty in azure and systematic uncertainty in blue.

### 777 2.2.2 Efficiency Correction

778 The interaction point for a track used in the total hadronic cross section analysis  
779 is defined to be the last point of the WC2TPC matched track which lies inside the  
780 fiducial volume. This definition is independent from the topology of the interaction.  
781 If the TPC track stops within the fiducial volume, its last point will be the interaction  
782 point, no matter what the products of the interaction look like; if the track crosses the  
783 boundaries of the fiducial volume, the track will be considered “through going” and no  
784 interaction point will be found. Given this definition, it is evident that we rely on the  
785 tracking algorithm to discern where the interaction occurred in the TPC and correctly  
786 stop the tracking. The tracking algorithm has an intrinsic angle resolution as shown  
787 in section 1.5.1, which limits its efficiency, especially in the case of elastic scattering  
788 occurring at low angles. Thus, we need to apply an efficiency correction to data in order  
789 to retrieve the true cross section. The efficiency correction is evaluated separately for  
790 the interacting and incident histograms, namely  $\epsilon_i^{\text{int}}$  and  $\epsilon_i^{\text{inc}}$ , and propagated to the  
791 cross section as shown in equation 9.

#### 792 Efficiency Correction: Procedure

793 We describe here the procedure to calculate the efficiency correction taking the in-  
794 teracting histogram as example and noting that the procedure is identical for the  
795 incident histogram.

796 We derive the correction on a set of pure pion MC, calculating its value bin by  
797 bin as the ratio between the true bin content and the correspondent reconstructed  
798 bin content. The correction is then applied to the relevant bin in data. In formulae,  
799 the efficiency correction is calculated to be

$$\epsilon^{\text{Int}}(E_i) = \frac{N_{\text{Interacting}}^{\pi \text{ Reco MC}}(E_i)}{N_{\text{Interacting}}^{\pi \text{ True MC}}(E_i)}, \quad (2.9)$$

where  $N_{\text{Int}}^{\pi \text{ True MC}}(E_i)$  is the content of the  $i$ -th bin in for the true interacting histogram, and  $N_{\text{Int}}^{\pi \text{ Reco MC}}(E_i)$  is the content of the  $i$ -th bin in for the reconstructed interacting histogram. The correction is applied to data as follows

$$N_{\text{Int}}^{\pi \text{ True Data}}(E_i) = \frac{N_{\text{Int}}^{\pi \text{ Reco Data}}(E_i)}{\epsilon^{\text{Int}}(E_i)} = N_{\text{Int}}^{\pi \text{ Reco Data}}(E_i) \frac{N_{\text{Int}}^{\pi \text{ True MC}}(E_i)}{N_{\text{Int}}^{\pi \text{ Reco MC}}(E_i)}. \quad (2.10)$$

where  $N_{\text{Int}}^{\pi \text{ Reco Data}}(E_i)$  is the background subtracted bin content of the  $i$ -th bin in for the reconstructed interacting histogram for data, i.e.

$$N_{\text{Int}}^{\pi \text{ Reco Data}}(E_i) = N_{\text{Int}}^{\text{TOT Data}}(E_i) - B_{\text{Int}}^{\text{Data}}(E_i) = C_{\text{Int}}^{\pi \text{ MC}}(E_i) N_{\text{Int}}^{\text{TOT Data}}(E_i). \quad (2.11)$$

In section 1.5.1, we estimated the angular resolution for data and MC to be  $\bar{\alpha}_{\text{Data}} = (5.0 \pm 4.5)$  deg and  $\bar{\alpha}_{\text{MC}} = (4.5 \pm 3.9)$  deg, respectively. Most interaction angles smaller than the angular resolution will thus be indistinguishable for the reconstruction. Thus, we claim we are able to measure the cross section for interaction angles greater than 5.0 deg. Geant4 simulates interactions at all angles, as shown in figure 2.7. In order to calculate the efficiency correction, we select events which have an interaction angle greater than a given  $\alpha_{\text{res}}$  to construct the true interacting and incident histograms (the denominator of the efficiency correction). The systematics on the efficiency correction is estimated by varying the value of  $\alpha_{\text{res}}$  between 0 deg and 4.5 deg and propagating the uncertainty on the cross section.

Figure 2.5 shows  $\epsilon^{\text{Int}}(E_i)$  in the left side and  $\epsilon^{\text{Inc}}(E_i)$  on the right as a function of the kinetic energy for the 60A runs and their systematic uncertainty. Similarly, figure 2.6 shows  $\epsilon^{\text{Int}}(E_i)$  in the left side and  $\epsilon^{\text{Inc}}(E_i)$  on the right as a function of the kinetic energy for the 100A runs and their systematic uncertainty.

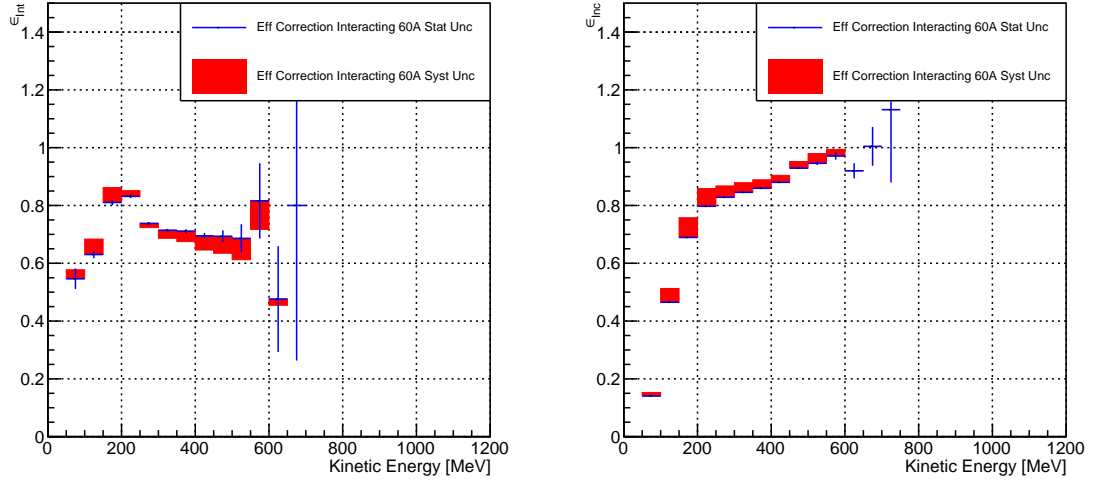


Figure 2.5: *Left:* Efficiency correction on the 60A interacting histogram, statistical uncertainty in blue, systematic uncertainty in red. *Right:* Efficiency correction on the 60A incident histogram, statistical uncertainty in blue, systematic uncertainty in red.

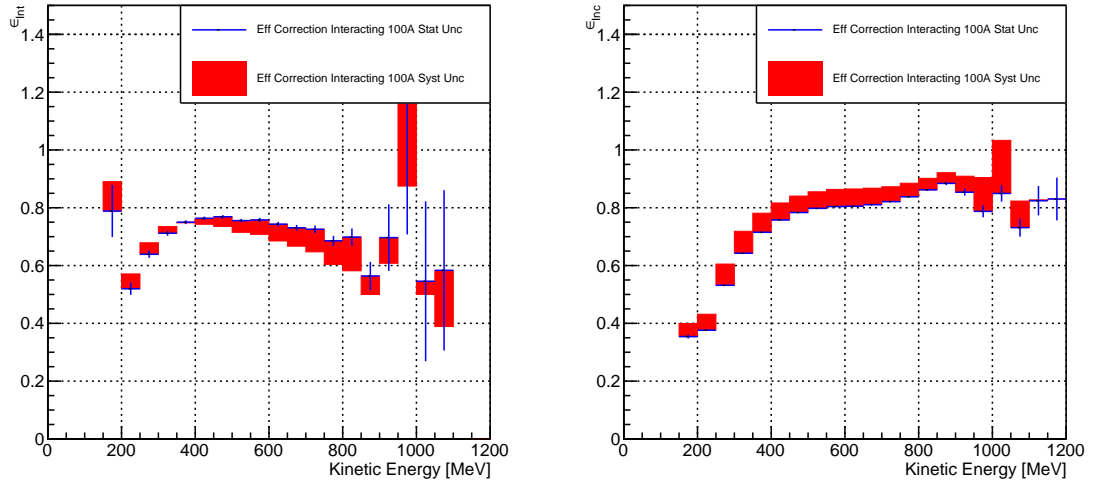


Figure 2.6: *Left:* Efficiency correction on the 100A interacting histogram, statistical uncertainty in blue, systematic uncertainty in red. *Right:* Efficiency correction on the 100A incident histogram, statistical uncertainty in blue, systematic uncertainty in red.

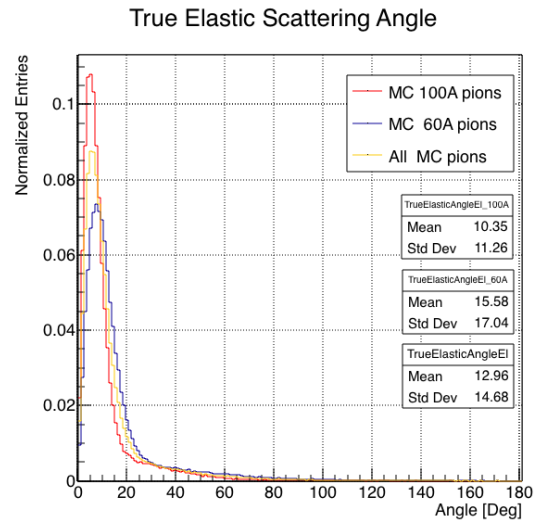


Figure 2.7: Distribution of the true scattering angle for a pion elastic scattering off the argon nucleus as simulated by Geant4.

## 2.3 Results

Figure 2.8 show the measurement of the ( $\pi^-$ -Ar) total hadronic cross section for scattering angles greater than  $5^\circ$ , as the result of the background subtraction and efficiency correction to the raw cross section. The top left plot is the measurement obtained on the 60A data, statistical uncertainty in black and systematic uncertainty in red. The top right plot is the measurement obtained on the 100A data, statistical uncertainty in black and systematic uncertainty in blue. The bottom plot shows the two measurements overlaid. In all three plot, the Geant4 prediction for the total hadronic cross section for angle scattering greater than  $5^\circ$  is displayed in green.

The systematic uncertainty on the cross section is the sum in quadrature of the statistical uncertainty, the systematic uncertainty related to the kinetic energy measurement, the systematic uncertainty related to the beam composition and the systematic uncertainty related to the efficiency correction.

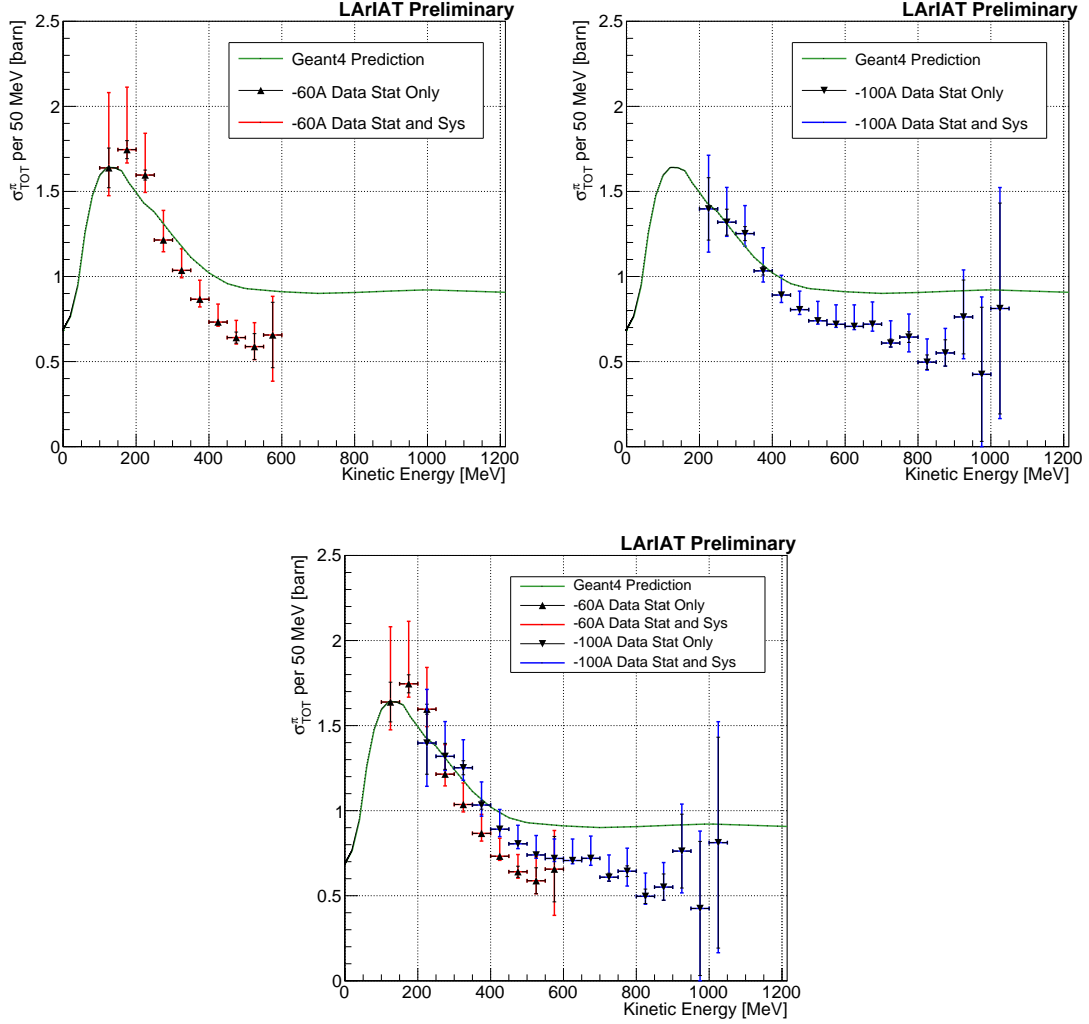


Figure 2.8: *Top Left:* ( $\pi^-$ -Ar) total hadronic cross section for scattering angles greater than  $5^\circ$  measured in the 60A sample, statistical uncertainty in black and systematic uncertainty in red. The Geant4 prediction for the total hadronic cross section for angle scattering greater than  $5^\circ$  is displayed in green.

*Top Right:* ( $\pi^-$ -Ar) total hadronic cross section for scattering angles greater than  $5^\circ$  measured in the 100A sample, statistical uncertainty in black and systematic uncertainty in blue. The Geant4 prediction for the total hadronic cross section for angle scattering greater than  $5^\circ$  is displayed in green.

*Bottom:* ( $\pi^-$ -Ar) total hadronic cross section measurements in the 60A and 100A samples overlaid with the Geant4 prediction (green).

## Chapter 3

# Positive Kaon Cross Section Measurement

In this chapter, we show the result of the thin slice method to measure the ( $K^+$ -Ar) total hadronic cross section. In Section 3.1, we start by measuring the raw cross section. In Section ??, we apply a statistical subtraction of the background contributions based on simulation and a correction for detection inefficiency. The final results are presented in Section ??.

### 3.1 Raw Cross Section

We measure the raw ( $K^+$ -Ar) total hadronic cross section as a function of the kinetic energy in the combined +60A and +100A dataset.

Similar to the pion case, the raw cross section is given by the equation 4

$$\sigma_{TOT}(E_i) = \frac{1}{n\delta X} \frac{N_{\text{Int}}^{\text{TOT}}(E_i)}{N_{\text{Inc}}^{\text{TOT}}(E_i)}, \quad (3.1)$$

where  $N_{\text{Int}}^{\text{TOT}}$  is the measured number of particles interacting at kinetic energy  $E_i$ ,  $N_{\text{Inc}}^{\text{TOT}}$  is the measured number of particles incident on an argon slice at kinetic energy



846  $E_i$ ,  $n$  is the density of the target centers and  $\delta X$  is the thickness of the argon slice.  
847 The density of the target centers and the slab thickness are  $n = 0.021 \cdot 10^{24} \text{ cm}^{-3}$  and  
848  $\delta X = 0.47 \text{ cm}$ , respectively.

849 As in the case of pions, kaons might decay or interact between WC4 and the  
850 TPC front face. Some of the interaction products may be wrongly matched to the  
851 WC track, forming the “secondary” particle’s background in the kaon sample. We  
852 estimate the effect of the contamination of secondaries thorough the DDMC kaon  
853 sample. Figure 3.1 shows the distribution of  $N_{\text{Int}}^{\text{TOT}}$  as a function of the kinetic energy.  
854 The data central points are represented by black dots, the statistical uncertainty is  
855 shown in black, while the systematic uncertainty is shown in red. Data is displayed  
856 over the  $N_{\text{Int}}^{\text{TOT}}$  distribution obtained with a DDMC sample of kaons shot from WC4.  
857 The contribution from the simulated kaons is shown in pink, the one from secondaries  
858 in red. The simulated kaon’s and secondaries’ contributions are stacked; the sum of  
859 their integrals is normalized to the integral of the data.

860 Figure 3.2 shows the distribution of  $N_{\text{Inc}}^{\text{TOT}}$ . Data is displayed over the MC. The  
861 same color scheme and normalization procedure is used for both the interacting and  
862 incident histograms.

863 Figure ?? shows the raw cross section, statistical uncertainty in black and system-  
864 atic uncertainty in red. The raw data cross section is overlaid to the reconstructed  
865 cross section for the MC mixed sample, displayed in azure. We calculate the sta-  
866 tistical uncertainty for the interacting, incident and cross section distributions in a  
867 similar fashion to the pion case as described in Section 2.1.1.

868 As in the pion case, the only systematic effect considered in the measurement of  
869 the raw cross section results from the propagation of the uncertainty associate with  
870 the measurement of the kinetic energy at each argon slab. For kaons, the uncertainty  
871 on the kinetic energy of a candidate at the  $j^{\text{th}}$  slab of argon is given by

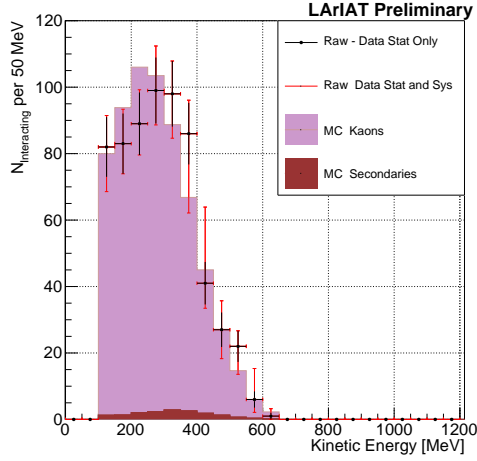


Figure 3.1: Raw number of interacting kaon candidates as a function of the reconstructed kinetic energy. The statistical uncertainties are shown in black, the systematic uncertainties in red.

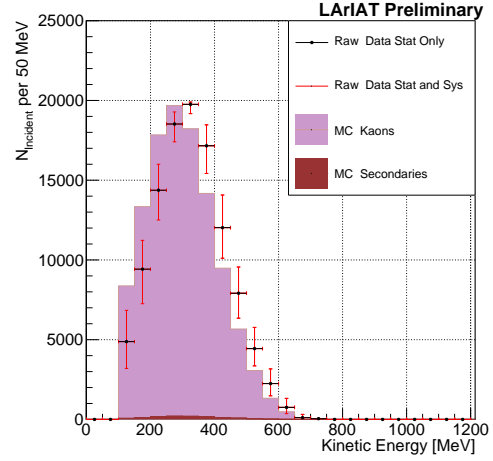


Figure 3.2: Raw number of incident kaon candidates as a function of the reconstructed kinetic energy. The statistical uncertainty is shown in black, the systematic uncertainties in red.

$$\delta KE_j = \sqrt{\delta p_{Beam}^2 + \delta E_{Loss}^2 + \delta E_{dep\ FF-j}^2} \quad (3.2)$$

$$= \sqrt{(2\% p_{Beam})^2 + (7 \text{ [MeV]})^2 + (j - 1)^2 (\sim 0.18 \text{ [MeV]})^2}. \quad (3.3)$$

872 We propagate this uncertainty by varying the energy measurement  $KE_j$  at each  
873 argon slab. We measure  $N_{Inc}^{TOT}$ ,  $N_{Int}^{TOT}$  and the cross section in three cases: first  
874 assigning the measured  $KE_j$  at each kinetic energy sampling, then assigning  $KE_j +$   
875  $\delta KE_j$ , and finally assigning  $KE_j - \delta KE_j$ . The difference between the values obtained  
876 using the  $KE_j$  sampling and the maximum and minimum values in each kinetic energy  
877 bin determines the systematic uncertainty.

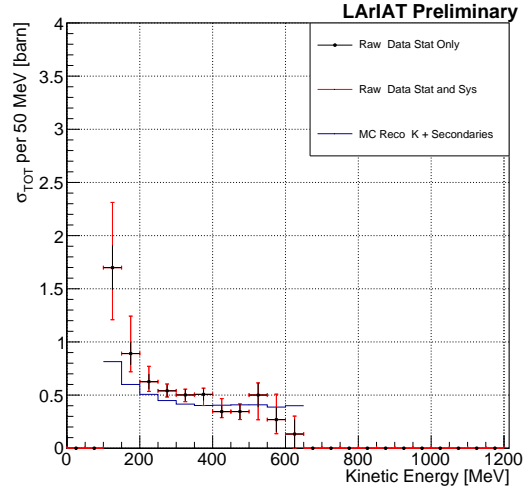


Figure 3.3: Raw ( $K^+$ -Ar) total hadronic cross section. The statistical uncertainty is shown in black, the systematic uncertainties in red. The raw cross section obtained with a MC sample of kaons is shown in azure. For the MC cross section, we include the contributions from secondaries.

## 878 **Appendix A**

# 879 **Additional Tracking Studies for** 880 **LArIAT Cross Section Analyses**

881 In this section, we describe two studies. The first is a justification of the selection  
882 criteria for the beamline handshake with the TPC information. We perform this  
883 study to boost the correct identification of the particles in the TPC associated with  
884 the beamline information, while maintaining sufficient statistics for the cross section  
885 measurement. The second study is an optimization of the tracking algorithm, with  
886 the scope of maximizing the identification of the hadronic interaction point inside the  
887 TPC. These two studies are related, since the optimization of the tracking is per-  
888 formed on TPC tracks which have been matched to the wire chamber track; in turn,  
889 the tracking algorithm for TPC tracks determines the number of reconstructed tracks  
890 in each event used to try the matching with the wire chamber track. Starting with  
891 a sensible tracking reconstruction, we perform the WC2TPC matching optimization  
892 first, then the tracking optimization. The WC2TPC match purity and efficiency are  
893 then calculated again with the optimized tracking.

## A.0.1 Study of WC to TPC Match

Plots I want in this section:

### 1. WC2TPC MC DeltaX, DeltaY and $\alpha$

Scope of this study is assessing the goodness of the wire chamber to TPC match on Monte Carlo and decide the selection values we will use on data. A word of caution is necessary here. With this study, we want to minimize pathologies associated with the presence of the primary hadron itself, e.g. the incorrect association between the beamline hadron and its decay products inside the TPC. Assessing the contamination from pile-up<sup>1</sup>, albeit related, is beyond the scope of this study.

In MC, we are able to define a correct WC2TPC match using the Geant4 truth information. We are thus able to count how many times the WC tracks is associated with the wrong TPC reconstructed track.

We define a correct match if the all following conditions are met:

- the length of the true primary Geant4 track in the TPC is greater than 2 cm,
- the length of the reconstructed track length is greater than 2 cm,
- the Z position of the first reconstructed point is within 2 cm from the TPC front face
- the distance between the reconstructed track and the true entering point is the minimum compared with all the other reconstructed tracks.

In order to count the wrong matches, we consider all the reconstructed tracks whose Z position of the first reconstructed point lies within 2 cm from the TPC front face. Events with true length in TPC  $< 2$  cm are included. Since hadrons are shot

---

1. We remind the reader that the DDMC is a single particle Monte Carlo, where the beam pile up is not simulated.

100 cm upstream from the TPC front face, the following two scenarios are possible from a truth standpoint:

- [ $Ta$ ] the primary hadron decays or interact strongly before getting to the TPC,
- [ $Tb$ ] the primary hadron enters the TPC.

As described in Section 0.2, we define a WC2TPC match according to the relative position of the WC and TPC track parametrized with  $\Delta R$  and the angle between them, parametrized with  $\alpha$ . Once we choose the selection values  $r_T$  and  $\alpha_T$  to determine a reconstructed WC2TPC match, the following five scenarios are possible in the truth to reconstruction interplay :

- 1) only the correct track is matched
- 2) only one wrong track is matched
- 3) the correct track and one (or more) wrong tracks are matched
- 4) multiple wrong tracks matched.
- 5) no reconstructed tracks are matched

Since we keep only events with one and only one match, we discard cases 3), 4) and 5) from the events used in the cross section measurement. For each set of  $r_T$  and  $\alpha_T$  selection value, we define purity and efficiency of the selection as follows:

$$\text{Efficiency} = \frac{\text{Number of events correctly matched}}{\text{Number of events with primary in TPC}}, \quad (\text{A.1})$$

$$\text{Purity} = \frac{\text{Number of events correctly matched}}{\text{Total number of matched events}}. \quad (\text{A.2})$$

Figure A.1 shows the efficiency (left) and purity (right) for WC2TPC match as a function of the radius,  $r_T$ , and angle,  $\alpha_T$ , selection value. It is apparent how both

935 efficiency and purity are fairly flat as a function of the radius selection value at a  
 936 given angle. This is not surprising. Since we are studying a single particle gun Monte  
 937 Carlo sample, the wrong matches can occur only for mis-tracking of the primary or  
 938 for association with decay products; decay products will tend to be produced at large  
 939 angles compared to the primary, but could be fairly close to the in  $x$  and  $y$  projection  
 940 of the primary. The radius cut would play a key role in removing pile up events.

941 For LArIAT cross section measurements, we generally prefer purity over efficiency,  
 942 since a sample of particles of a pure species will lead to a better measurement. Ob-  
 943 viously, purity should be balanced with a sensible efficiency to avoid rejecting the  
 944 whole sample.

945 We choose  $(\alpha_T, r_T) = (8 \text{ deg}, 4 \text{ cm})$  and get a MC 85% efficiency and 98% purity  
 946 for the kaon sample and a MC 95% efficiency and 90% purity for the pion sample.

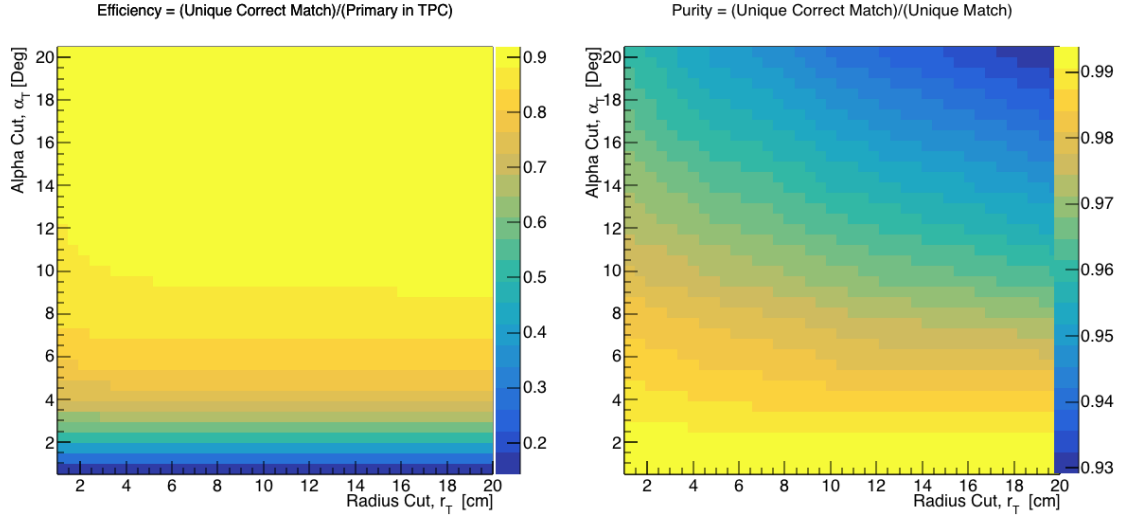


Figure A.1: Efficiency (left) and purity (right) for WC2TPC match as a function of the radius and angle selections for the kaon sample.

## 947 A.0.2 Tracking Optimization

## Appendix B

### Energy Calibration

Scope of the energy calibration is to identify the factors which convert the charge collected (dQ) to energy deposited in the chamber (dE). As described in section ??, this is a multi-step procedure. In LArIAT, we first correct the raw charge by the electronic noise on the considered wire [102], then by the electron lifetime [103], and then by the recombination using the ArgoNeut recombination values. Lastly, we apply overall calibration of the energy, i.e. we determine the “calorimetry constants” using the procedure described in this section.

We independently determine the calorimetry constants for Data and Monte Carlo in the LArIAT Run-II Data samples using a parametrization of the stopping power (a.k.a. energy deposited per unit length,  $dE/dX$ ) as a function of momentum. This is done by comparing the stopping power measured on reconstructed quantities against the Bethe-Bloch theoretical prediction for various particle species (see Equation ??). We obtain the theoretical expectation for the  $dE/dX$  most probable value of pions ( $\pi$ ), muons ( $\mu$ ), kaons ( $K$ ), and protons ( $p$ ) in the momentum range most relevant for LArIAT (Figure B.1) using the tables provided by the Particle Data Group [100] for liquid argon [1].

The basic idea of this calibration technique is to utilize a sample of beamline



events with known particle species and momentum to measure the  $dE/dX$  of the corresponding tracks in the TPC. In particular, we decided to use positive pions as calibration sample and samples from all the other particle species as cross check. Once the  $dE/dX$  of the positive pion sample has been measured at various momenta, we tune to calorimetry constants within the reconstruction software to align the measured values to match the theoretical ones found in Figure B.1.

In data, we start by selecting a sample of beamline positive pion beamline candidates without any restriction on their measured momentum<sup>1</sup>. We then apply the WC2TPC match and subtract the energy loss upstream to the TPC front face, determining the momentum at the TPC front face. For each surviving pion candidate, we measure the  $dE/dx$  at each of the first 12 spacepoints associated the 3D reconstructed track, corresponding to a  $\sim 5$  cm portion. These  $dE/dX$  measurements are then put into a histogram that corresponds to measured momentum of the track. The  $dE/dX$  histograms are sampled every 50 MeV/c in momentum (e.g. 150 MeV/c  $< P < 200$  MeV/c, 200 MeV/c  $< P < 250$  MeV/c, etc...). This process of selecting, sampling, and recording the  $dE/dX$  for various momentum bins is repeated over the entire sample of events, allowing us to collect sufficient statistic in most of the momentum bins between 150 MeV/c and 1100 MeV/c. On average, pions and muons only lose  $\sim 10$  MeV in this 5 cm section of the track and protons lose  $\sim 20$  MeV. Thus choosing 50 MeV/c size bins for our histograms covers the energy spread within those bins due to energy loss from ionization for all the particle species identifiable in the beamline. Each 50 MeV/c momentum binned  $dE/dX$  histogram is now fit with a simple Landau function. The most probable value (MPV) and the associated error on the MPV from the fit are extracted and plotted against the theoretical prediction Figure B.1. Depending on the outcome of the data-prediction comparison, we modify the calorimetry constants and we repeat the procedure until a qualitative agreement

---

1. it should be noted that some muon and positron contamination is present in the  $\pi^+$  sample

993 is achieved. We perform this tuning for the collection and induction plane separately.  
 994 As a cross check to the calorimetry constants determined using the positive pions,  
 995 we lock the constants and plot the  $dE/dx$  versus momentum distribution of all the  
 996 other particle species identifiable in the beamline data ( $\pi/\mu/e$ , K , p, in both polari-  
 997 ties) against the corresponding Beth-Bloch prediction. The agreement between data  
 998 from the other particle species and the predictions is the expected result of this cross  
 999 check. The results of the tuning and cross check for Run-II data on the collection  
 1000 plane is shown in Figure B.2 negative polarity data on top, positive polarity data on  
 1001 the bottom.

1002 In MC, we simulate the corresponding positive pion sample with the DDMC (see  
 1003 section 1.2.2) and follow the same steps as in data. More details on the calorimetry  
 1004 tuning can be found in [78].

1005 Add agreement between data and MC for dedx for pions

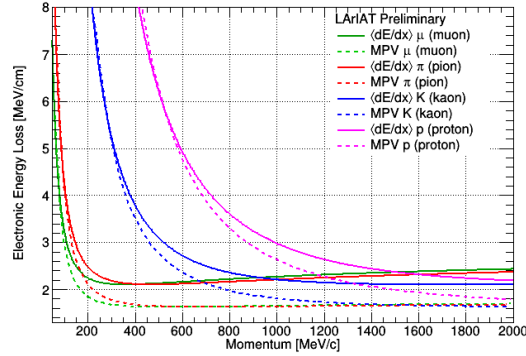


Figure B.1: Stopping power for pions, muons, kaons, and protons in liquid argon over the momentum range most relevant for LArIAT according to the Beth-Bloch equation. The solid lines represent the prediction for the mean energy  $dE/dX$ , while the dashed lines are the predictions for the MPV.

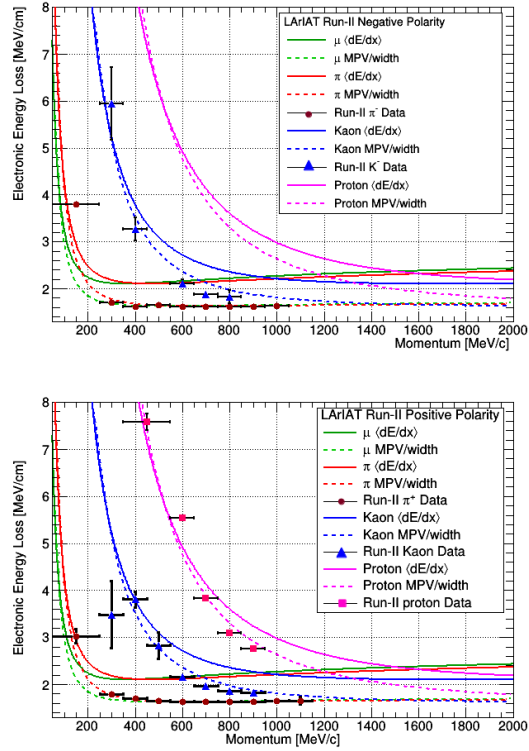


Figure B.2: Stopping power versus Momentum for Run-II negative (top) and positive (bottom) polarity data. We achieve the agreement between the Bethe-Bloch predictions and the distribution obtained with of the positive pions (top plot, red dots) by tuning the calorimetry constants. Once the calorimetry constants are locked in, the agreement between the other particle species and the Bethe-Bloch predictions follows naturally.

## 1006 Appendix C

# 1007 Measurement of LArIAT Electric 1008 Field

1009 The electric field of a LArTPC in the drift volume is a fundamental quantity for  
1010 the proper functionality of this technology, as it affects almost every reconstructed  
1011 quantity such as the position of hits or their collected charge. Given its importance,  
1012 we calculate the electric field for LArIAT with a single line diagram from our HV  
1013 circuit and we cross check the obtained value with a measurement relying only on  
1014 TPC data.

1015 Before getting into the details of the measurement procedures, it is important to  
1016 explicit the relationship between some quantities in play. The electric field and the  
1017 drift velocity ( $v_{drift}$ ) are related as follows

$$v_{drift} = \mu(E_{field}, T)E_{field}, \quad (C.1)$$

1018 where  $\mu$  is the electron mobility, which depends on the electric field and on the  
1019 temperature (T). The empirical formula for this dependency is described in [?] and  
1020 shown in Figure C.1 for several argon temperatures.

1021 The relationship between the drift time ( $t_{drift}$ ) and the drift velocity is trivially

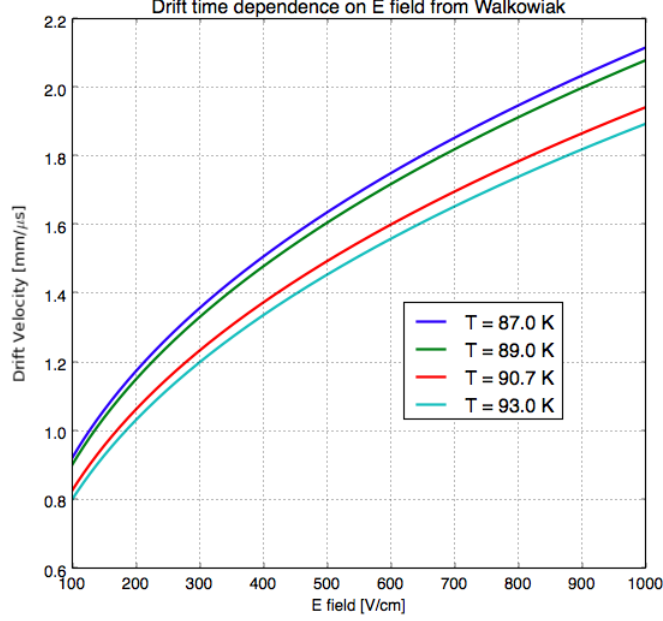


Figure C.1: Drift velocity dependence on electric field for several temperatures. The slope of the line at any one point represents the electron mobility for that given temperature and electric field.

Table C.1: Electric field and drift velocities in LArIAT smaller drift volumes

	Shield-Induction	Induction-Collection
$E_{field}$	700.63 V/cm	892.5 V/cm
$v_{drift}$	1.73 mm/ $\mu$ s	1.90 mm/ $\mu$ s
$t_{drift}$	2.31 $\mu$ s	2.11 $\mu$ s

1022 given by

$$t_{drift} = \Delta x / v_{drift}, \quad (C.2)$$

1023 where  $\Delta x$  is the distance between the edges of the drift region. Table C.1 reports the  
 1024 values of the electric field, drift velocity, and drift times for the smaller drift volumes.

1025 With these basic parameters established, we can now move on to calculating the  
 1026 electric field in the main drift region (between the cathode and the shield plane).

## Single line diagram method

The electric field strength in the LArIAT main drift volume can be determined knowing the voltage applied to the cathode, the voltage applied at the shield plane, and the distance between them. We assume the distance between the cathode and the shield plane to be 470 mm and any length contraction due to the liquid argon is negligibly small ( $\sim 2$  mm).

The voltage applied to the cathode can be calculated using Ohm's law and the single line diagram shown in Figure C.2. A set of two of filter pots for emergency power dissipation are positioned between the Glassman power supply and the cathode, one at each end of the feeder cable, each with an internal resistance of  $40\text{ M}\Omega$ .

Given the TPC resistor chain, the total TPC impedance is  $6\text{ G}\Omega$ . Since the total resistance on the circuit is driven by the TPC impedance, we expect the resulting current to be

$$I = V_{PS}/R_{tot} = -23.5\text{ kV}/6\text{ G}\Omega \sim 4\text{ }\mu\text{A}, \quad (\text{C.3})$$

which we measure with the Glassman power supply, shown in Figure C.3.

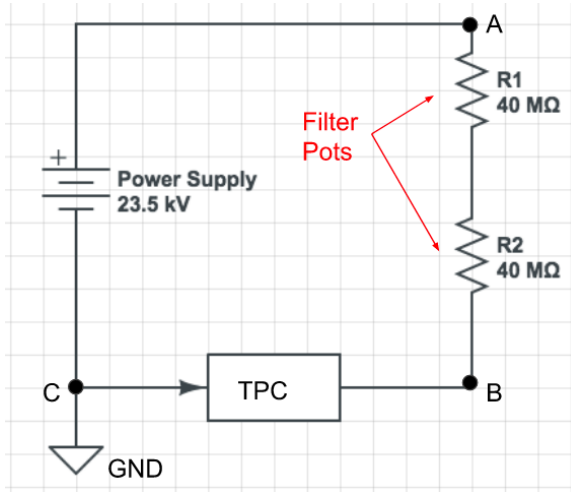


Figure C.2: LArIAT HV simple schematics.

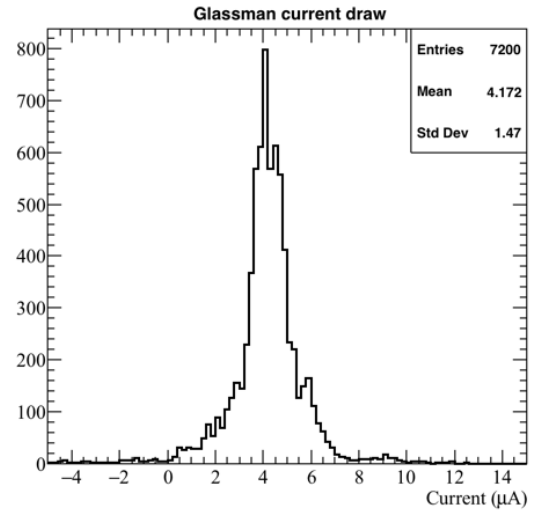


Figure C.3: Current reading from the Glassman between May 25th and May 30th, 2016 (typical Run-II conditions).

1041 Using this current, the voltage at the cathode is calculated as

$$V_{BC} = V_{PS} - (I \times R_{eq}) = -23.5 \text{ kV} + (0.00417 \text{ mA} \times 80 \text{ M}\Omega) = -23.17 \text{ kV}, \quad (\text{C.4})$$

1042 where  $I$  is the current and  $R_{eq}$  is the equivalent resistor representing the two filter  
1043 pots. The electric field is then calculated to be

$$E_{\text{field}} = \frac{V_{BC} - V_{\text{shield}}}{\Delta x} = 486.54 \text{ V/cm}. \quad (\text{C.5})$$

## 1044 **E field using cathode-anode piercing tracks**

1045 We devise an independent method to measure the drift time (and consequently drift  
1046 velocity and electric field) using TPC cathode to anode piercing tracks. We use this  
1047 method as a cross check to the single line method. The basic idea is simple:

- 1048 0. Select cosmic ray events with only 1 reconstructed track
- 1049 1. Reduce the events to the one containing tracks that cross both anode and cath-  
1050 ode
- 1051 2. Identify the first and last hit of the track
- 1052 3. Measure the time difference between these two hits ( $\Delta t$ ).

1053 This method works under the assumptions that the time it takes for a cosmic particle  
1054 to cross the chamber ( $\sim \text{ns}$ ) is small compared to the charge drift time ( $\sim \text{hundreds}$   
1055 of  $\mu\text{s}$ ).

1056 We choose cosmic events to allow for a high number of anode to cathode piercing  
1057 tracks (ACP tracks), rejecting beam events where the particles travel almost perpen-  
1058 dicularly to drift direction. We select events with only one reconstructed track to  
1059 maximize the chance of selecting a single crossing muon (no-michel electron). We  
1060 utilize ACP tracks because their hits span the full drift length of the TPC, see figure

1061 C.4, allowing us to define where the first and last hit of the tracks are located in space  
1062 regardless of our assumption of the electric field.

1063 One of the main features of this method is that it doesn't rely on the measurement  
1064 of the trigger time. Since  $\Delta t$  is the time difference between the first and last hit of a  
1065 track and we assume the charge started drifting at the same time for both hits, the  
1066 measurement of the absolute beginning of drift time  $t_0$  is unnecessary. We boost the  
1067 presence of ACP tracks in the cosmic sample by imposing the following requirements  
1068 on tracks:

- 1069 • vertical position (Y) of first and last hits within  $\pm 18$  cm from TPC center  
1070 (avoid Top-Bottom tracks)
- 1071 • horizontal position (Z) of first and last hits within 2 and 86 cm from TPC front  
1072 face (avoid through going tracks)
- 1073 • track length greater than 48 cm (more likely to be crossing)
- 1074 • angle from the drift direction (phi in figure C.5) smaller than 50 deg (more  
1075 reliable tracking)
- 1076 • angle from the beam direction (theta in figure C.5) greater than 50 deg (more  
1077 reliable tracking)

1078 Tracks passing all these selection requirements are used for the  $\Delta t$  calculation.

1079 For each track passing our selection, we loop through the associated hits to retrieve  
1080 the timing information. The analysis is performed separately on hits on the collection  
1081 plane and induction plane, but lead to consistent results. As an example of the time  
1082 difference, figures C.6 and C.7 represent the difference in time between the last and  
1083 first hit of the selected tracks for Run-II Positive Polarity sample on the collection  
1084 and induction plane respectively. We fit with a Gaussian to the peak of the  $\Delta t$   
1085 distributions to extract the mean drift time and the uncertainty associated with it.



1086 The long tail at low  $\Delta t$  represents contamination of non-ACP tracks in the track  
 1087 selection. We apply the same procedure to Run-I and Run-II, positive and negative  
 1088 polarity alike.

1089 To convert  $\Delta t$  recorded for the hits on the induction plane to the drift time we  
 1090 employ the formula

$$t_{drift} = \Delta t - t_{S-I} \quad (C.6)$$

1091 where  $t_{drift}$  is the time the charge takes to drift in the main volume between the  
 1092 cathode and the shield plane and  $t_{S-I}$  is the time it takes for the charge to drift from  
 1093 the shield plane to the induction plane. In Table C.1 we calculated the drift velocity  
 1094 in the S-I region, thus we can calculate  $t_{S-I}$  as

$$t_{S-I} = \frac{l_{S-I}}{v_{S-I}} = \frac{4mm}{1.73mm/\mu s} \quad (C.7)$$

1095 where  $l_{S-I}$  is the distance between the shield and induction plane and  $v_{S-I}$  is the drift  
 1096 velocity in the same region. A completely analogous procedure is followed for the hits  
 1097 on the collection plane, taking into account the time the charge spent in drifting from  
 1098 shield to induction as well as between the induction and collection plane. The value  
 1099 for  $\Delta t_{drift}$ , the calculated drift velocity ( $v_{drift}$ ), and corresponding drift electric field  
 1100 for the various run periods is given in Table C.2 and are consistent with the electric  
 1101 field value calculated with the single line diagram method.

**Delta  $t_{drift}$ , drift  $v$  and E field with ACP tracks**

Data Period	$\Delta t_{Drift} [\mu s]$	Drift velocity $[mm/\mu s]$	E field $[V/cm]$
RunI Positive Polarity Induction	$311.1 \pm 2.4$	$1.51 \pm 0.01$	$486.6 \pm 21$
RunI Positive Polarity Collection	$310.9 \pm 2.6$	$1.51 \pm 0.01$	$487.2 \pm 21$
RunII Positive Polarity Induction	$315.7 \pm 2.8$	$1.49 \pm 0.01$	$467.9 \pm 21$
RunII Positive Polarity Collection	$315.7 \pm 2.7$	$1.49 \pm 0.01$	$467.9 \pm 21$
RunII Negative Polarity Induction	$315.9 \pm 2.6$	$1.49 \pm 0.01$	$467.1 \pm 21$
RunII Negative Polarity Collection	$315.1 \pm 2.8$	$1.49 \pm 0.01$	$470.3 \pm 21$
Average Values	314.1	$1.50 \pm 0.01$	$474.3 \pm 21$

Table C.2:  $\Delta t$  for the different data samples used for the Anode-Cathode Piercing tracks study.

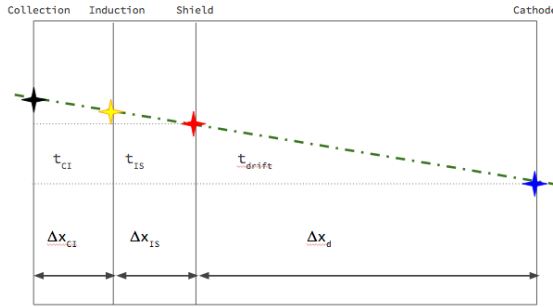


Figure C.4: Pictorial representation of the YX view of the TPC. The distance within the anode planes and between the shield plane and the cathode is purposely out of proportion to illustrate the time difference between hits on collection and induction. An ACP track is shown as an example.

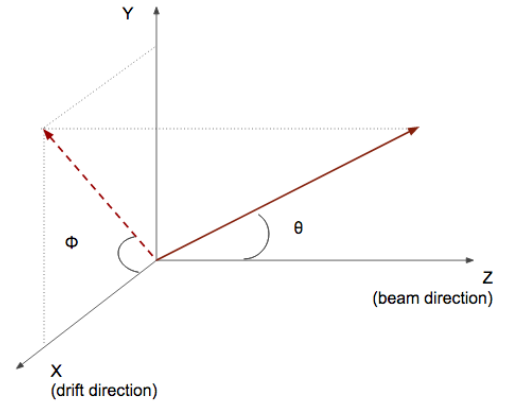


Figure C.5: Angle definition in the context of LArIAT coordinate system.

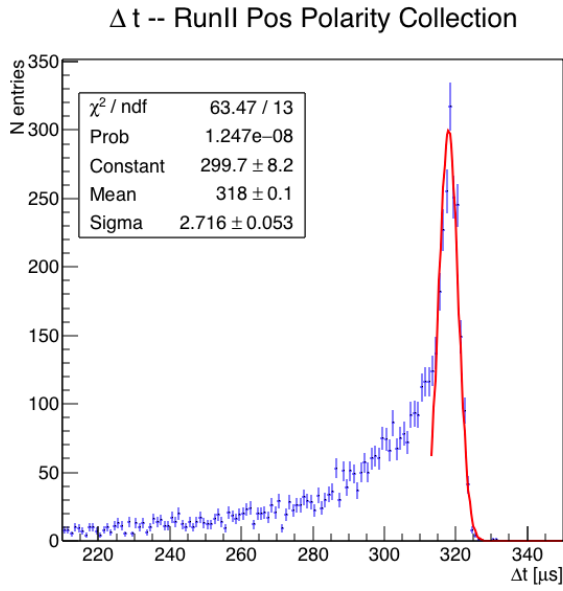


Figure C.6: Collection plane  $\Delta t$  fit for Run II positive polarity ACP data selected tracks.

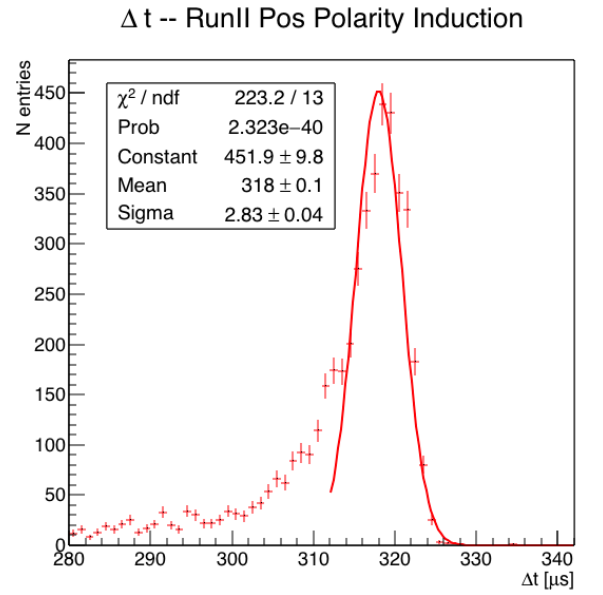


Figure C.7: Induction plane  $\Delta t$  fit for Run II positive polarity ACP data selected tracks.

# 1102 Bibliography

- 1103 [1] PDG Tables for Liquid Argon. . Technical report.
- 1104 [2] Precision electroweak measurements on the  $z$  resonance. *Physics Reports*,  
1105 427(5):257 – 454, 2006.
- 1106 [3] K. Abe, J. Amey, C. Andreopoulos, M. Antonova, S. Aoki, A. Ariga, D. Au-  
1107 tiero, S. Ban, M. Barbi, G. J. Barker, G. Barr, C. Barry, P. Bartet-Friburg,  
1108 M. Batkiewicz, V. Berardi, S. Berkman, S. Bhadra, S. Bienstock, A. Blondel,  
1109 S. Bolognesi, S. Bordoni, S. B. Boyd, D. Brailsford, A. Bravar, C. Bronner,  
1110 M. Buizza Avanzini, R. G. Calland, T. Campbell, S. Cao, S. L. Cartwright,  
1111 M. G. Catanesi, A. Cervera, C. Checchia, D. Cherdack, N. Chikuma,  
1112 G. Christodoulou, A. Clifton, J. Coleman, G. Collazuol, D. Coplowe, A. Cudd,  
1113 A. Dabrowska, G. De Rosa, T. Dealtry, P. F. Denner, S. R. Dennis, C. Densham,  
1114 D. Dewhurst, F. Di Lodovico, S. Di Luise, S. Dolan, O. Drapier, K. E. Duffy,  
1115 J. Dumarchez, M. Dziewiecki, S. Emery-Schrenk, A. Ereditato, T. Feusels,  
1116 A. J. Finch, G. A. Fiorentini, M. Friend, Y. Fujii, D. Fukuda, Y. Fukuda,  
1117 V. Galymov, A. Garcia, C. Giganti, F. Gizzarelli, T. Golan, M. Gonin, D. R.  
1118 Hadley, L. Haegel, M. D. Haigh, D. Hansen, J. Harada, M. Hartz, T. Hasegawa,  
1119 N. C. Hastings, T. Hayashino, Y. Hayato, R. L. Helmer, A. Hillairet, T. Hiraki,  
1120 A. Hiramoto, S. Hirota, M. Hogan, J. Holeczek, F. Hosomi, K. Huang, A. K.  
1121 Ichikawa, M. Ikeda, J. Imber, J. Insler, R. A. Intonti, T. Ishida, T. Ishii, E. Iwai,  
1122 K. Iwamoto, A. Izmaylov, B. Jamieson, M. Jiang, S. Johnson, P. Jonsson,

1123 C. K. Jung, M. Kabirnezhad, A. C. Kaboth, T. Kajita, H. Kakuno, J. Kameda,  
 1124 D. Karlen, T. Katori, E. Kearns, M. Khabibullin, A. Khotjantsev, H. Kim,  
 1125 J. Kim, S. King, J. Kisiel, A. Knight, A. Knox, T. Kobayashi, L. Koch, T. Koga,  
 1126 A. Konaka, K. Kondo, L. L. Kormos, A. Korzenev, Y. Koshio, K. Kowalik,  
 1127 W. Kropp, Y. Kudenko, R. Kurjata, T. Kutter, J. Lagoda, I. Lamont, M. Lam-  
 1128 oureux, E. Larkin, P. Lasorak, M. Laveder, M. Lawe, M. Licciardi, T. Lindner,  
 1129 Z. J. Liptak, R. P. Litchfield, X. Li, A. Longhin, J. P. Lopez, T. Lou, L. Ludovici,  
 1130 X. Lu, L. Magaletti, K. Mahn, M. Malek, S. Manly, A. D. Marino, J. F. Martin,  
 1131 P. Martins, S. Martynenko, T. Maruyama, V. Matveev, K. Mavrokoridis, W. Y.  
 1132 Ma, E. Mazzucato, M. McCarthy, N. McCauley, K. S. McFarland, C. McGrew,  
 1133 A. Mefodiev, C. Metelko, M. Mezzetto, P. Mijakowski, A. Minamino, O. Mi-  
 1134 neev, S. Mine, A. Missert, M. Miura, S. Moriyama, Th. A. Mueller, J. Myslik,  
 1135 T. Nakadaira, M. Nakahata, K. G. Nakamura, K. Nakamura, K. D. Nakamura,  
 1136 Y. Nakanishi, S. Nakayama, T. Nakaya, K. Nakayoshi, C. Nantais, C. Nielsen,  
 1137 M. Nirkko, K. Nishikawa, Y. Nishimura, P. Novella, J. Nowak, H. M. O’Keeffe,  
 1138 K. Okumura, T. Okusawa, W. Oryszczak, S. M. Oser, T. Ovsyannikova, R. A.  
 1139 Owen, Y. Oyama, V. Palladino, J. L. Palomino, V. Paolone, N. D. Patel,  
 1140 P. Paudyal, M. Pavin, D. Payne, J. D. Perkin, Y. Petrov, L. Pickard, L. Pick-  
 1141 ering, E. S. Pinzon Guerra, C. Pistillo, B. Popov, M. Posiadala-Zezula, J.-M.  
 1142 Poutissou, R. Poutissou, P. Przewlocki, B. Quilain, T. Radermacher, E. Radi-  
 1143 cioni, P. N. Ratoff, M. Ravonel, M. A. Rayner, A. Redij, E. Reinherz-Aronis,  
 1144 C. Riccio, P. A. Rodrigues, E. Rondio, B. Rossi, S. Roth, A. Rubbia, A. Rychter,  
 1145 K. Sakashita, F. Sánchez, E. Scantamburlo, K. Scholberg, J. Schwehr, M. Scott,  
 1146 Y. Seiya, T. Sekiguchi, H. Sekiya, D. Sgalaberna, R. Shah, A. Shaikhiev,  
 1147 F. Shaker, D. Shaw, M. Shiozawa, T. Shirahige, S. Short, M. Smy, J. T.  
 1148 Sobczyk, H. Sobel, M. Sorel, L. Southwell, J. Steinmann, T. Stewart, P. Stowell,  
 1149 Y. Suda, S. Suvorov, A. Suzuki, S. Y. Suzuki, Y. Suzuki, R. Tacik, M. Tada,

1150 A. Takeda, Y. Takeuchi, H. K. Tanaka, H. A. Tanaka, D. Terhorst, R. Terri,  
 1151 T. Thakore, L. F. Thompson, S. Tobayama, W. Toki, T. Tomura, C. Tourama-  
 1152 nis, T. Tsukamoto, M. Tzanov, Y. Uchida, M. Vagins, Z. Vallari, G. Vasseur,  
 1153 T. Vladisavljevic, T. Wachala, C. W. Walter, D. Wark, M. O. Wascko, A. We-  
 1154 ber, R. Wendell, R. J. Wilkes, M. J. Wilking, C. Wilkinson, J. R. Wilson, R. J.  
 1155 Wilson, C. Wret, Y. Yamada, K. Yamamoto, M. Yamamoto, C. Yanagisawa,  
 1156 T. Yano, S. Yen, N. Yershov, M. Yokoyama, K. Yoshida, T. Yuan, M. Yu, A. Za-  
 1157 lewska, J. Zalipska, L. Zambelli, K. Zaremba, M. Ziembicki, E. D. Zimmerman,  
 1158 M. Zito, and J. Żmuda. Combined analysis of neutrino and antineutrino oscil-  
 1159 lations at t2k. *Phys. Rev. Lett.*, 118:151801, Apr 2017.

1160 [4] K. Abe, Y. Haga, Y. Hayato, M. Ikeda, K. Iyogi, J. Kameda, Y. Kishimoto,  
 1161 M. Miura, S. Moriyama, M. Nakahata, T. Nakajima, Y. Nakano, S. Nakayama,  
 1162 A. Orii, H. Sekiya, M. Shiozawa, A. Takeda, H. Tanaka, T. Tomura, R. A. Wen-  
 1163 dell, R. Akutsu, T. Irvine, T. Kajita, K. Kaneyuki, Y. Nishimura, E. Richard,  
 1164 K. Okumura, L. Labarga, P. Fernandez, J. Gustafson, C. Kachulis, E. Kearns,  
 1165 J. L. Raaf, J. L. Stone, L. R. Sulak, S. Berkman, C. M. Nantais, H. A.  
 1166 Tanaka, S. Tobayama, M. Goldhaber, W. R. Kropp, S. Mine, P. Weatherly,  
 1167 M. B. Smy, H. W. Sobel, V. Takhistov, K. S. Ganezer, B. L. Hartfiel, J. Hill,  
 1168 N. Hong, J. Y. Kim, I. T. Lim, R. G. Park, A. Himmel, Z. Li, E. O’Sullivan,  
 1169 K. Scholberg, C. W. Walter, T. Wongjirad, T. Ishizuka, S. Tasaka, J. S. Jang,  
 1170 J. G. Learned, S. Matsuno, S. N. Smith, M. Friend, T. Hasegawa, T. Ishida,  
 1171 T. Ishii, T. Kobayashi, T. Nakadaira, K. Nakamura, Y. Oyama, K. Sakashita,  
 1172 T. Sekiguchi, T. Tsukamoto, A. T. Suzuki, Y. Takeuchi, T. Yano, S. V. Cao,  
 1173 T. Hiraki, S. Hirota, K. Huang, T. Kikawa, A. Minamino, T. Nakaya, K. Suzuki,  
 1174 Y. Fukuda, K. Choi, Y. Itow, T. Suzuki, P. Mijakowski, K. Frankiewicz, J. Hig-  
 1175 night, J. Imber, C. K. Jung, X. Li, J. L. Palomino, M. J. Wilking, C. Yanag-  
 1176 isawa, D. Fukuda, H. Ishino, T. Kayano, A. Kibayashi, Y. Koshio, T. Mori,

1177 M. Sakuda, C. Xu, Y. Kuno, R. Tacik, S. B. Kim, H. Okazawa, Y. Choi,  
1178 K. Nishijima, M. Koshihara, Y. Totsuka, Y. Suda, M. Yokoyama, C. Bronner,  
1179 M. Hartz, K. Martens, Ll. Marti, Y. Suzuki, M. R. Vagins, J. F. Martin, A. Kon-  
1180 aka, S. Chen, Y. Zhang, and R. J. Wilkes. Search for proton decay via  $p \rightarrow e^+ \pi^0$   
1181 and  $p \rightarrow \mu^+ \pi^0$  in 0.31 megaton  $\cdot$  years exposure of the super-kamiokande water  
1182 cherenkov detector. *Phys. Rev. D*, 95:012004, Jan 2017.

1183 [5] R Acciarri, C Adams, J Asaadi, B Baller, T Bolton, C Bromberg, F Ca-  
1184 vanna, E Church, D Edmunds, A Ereditato, S Farooq, B Fleming, H Greenlee,  
1185 G Horton-Smith, C James, E Klein, K Lang, P Laurens, D McKee, R Mehdiyev,  
1186 B Page, O Palamara, K Partyka, G Rameika, B Rebel, M Soderberg, J Spitz,  
1187 A M Szelc, M Weber, M Wojcik, T Yang, and G P Zeller. A study of electron  
1188 recombination using highly ionizing particles in the argoneut liquid argon tpc.  
1189 *Journal of Instrumentation*, 8(08):P08005, 2013.

1190 [6] R Acciarri, M Antonello, B Baibussinov, M Baldo-Ceolin, P Benetti,  
1191 F Calaprice, E Calligarich, M Cambiaghi, N Canci, F Carbonara, F Cavanna,  
1192 S Centro, A G Cocco, F Di Pompeo, G Fiorillo, C Galbiati, V Gallo, L Grandi,  
1193 G Meng, I Modena, C Montanari, O Palamara, L Pandola, G B Piano Mortari,  
1194 F Pietropaolo, G L Raselli, M Roncadelli, M Rossella, C Rubbia, E Segreto,  
1195 A M Szelc, S Ventura, and C Vignoli. Effects of nitrogen contamination in  
1196 liquid argon. *Journal of Instrumentation*, 5(06):P06003, 2010.

1197 [7] R. Acciarri et al. Demonstration and Comparison of Operation of Photomulti-  
1198 plier Tubes at Liquid Argon Temperature. *JINST*, 7:P01016, 2012.

1199 [8] R. Acciarri et al. Design and Construction of the MicroBooNE Detector. *JINST*,  
1200 12(02):P02017, 2017.

- [9] R. Acciarri et al. First Observation of Low Energy Electron Neutrinos in a Liquid Argon Time Projection Chamber. *Phys. Rev.*, D95(7):072005, 2017. [Phys. Rev.D95,072005(2017)].
- [10] M Adamowski, B Carls, E Dvorak, A Hahn, W Jaskierny, C Johnson, H Jostlein, C Kendziora, S Lockwitz, B Pahlka, R Plunkett, S Pordes, B Rebel, R Schmitt, M Stancari, T Tope, E Voirin, and T Yang. The liquid argon purity demonstrator. *Journal of Instrumentation*, 9(07):P07005, 2014.
- [11] C. Adams et al. The Long-Baseline Neutrino Experiment: Exploring Fundamental Symmetries of the Universe. 2013.
- [12] P. Adamson, L. Aliaga, D. Ambrose, N. Anfimov, A. Antoshkin, E. Arrieta-Diaz, K. Augsten, A. Aurisano, C. Backhouse, M. Baird, B. A. Bambah, K. Bays, B. Behera, S. Bending, R. Bernstein, V. Bhatnagar, B. Bhuyan, J. Bian, T. Blackburn, A. Bolshakova, C. Bromberg, J. Brown, G. Brunetti, N. Buchanan, A. Butkevich, V. Bychkov, M. Campbell, E. Catano-Mur, S. Childress, B. C. Choudhary, B. Chowdhury, T. E. Coan, J. A. B. Coelho, M. Colo, J. Cooper, L. Corwin, L. Cremonesi, D. Cronin-Hennessy, G. S. Davies, J. P. Davies, P. F. Derwent, R. Dharmapalan, P. Ding, Z. Djurcic, E. C. Dukes, H. Duyang, S. Edayath, R. Ehrlich, G. J. Feldman, M. J. Frank, M. Gabrielyan, H. R. Gallagher, S. Germani, T. Ghosh, A. Giri, R. A. Gomes, M. C. Goodman, V. Grichine, R. Group, D. Grover, B. Guo, A. Habig, J. Hartnell, R. Hatcher, A. Hatzikoutelis, K. Heller, A. Himmel, A. Holin, J. Hylen, F. Jediny, M. Judah, G. K. Kafka, D. Kalra, S. M. S. Kasahara, S. Kasetti, R. Keloth, L. Kolupaeva, S. Kotelnikov, I. Kourbanis, A. Kreymer, A. Kumar, S. Kurbanov, K. Lang, W. M. Lee, S. Lin, J. Liu, M. Lokajicek, J. Lozier, S. Luchuk, K. Maan, S. Magill, W. A. Mann, M. L. Marshak, K. Matera, V. Matveev, D. P. Méndez, M. D. Messier, H. Meyer, T. Miao, W. H. Miller, S. R. Mishra, R. Mohanta, A. Moren,



1227 L. Mualem, M. Muether, S. Mufson, R. Murphy, J. Musser, J. K. Nelson,  
 1228 R. Nichol, E. Niner, A. Norman, T. Nosek, Y. Oksuzian, A. Olshevskiy, T. Ol-  
 1229 son, J. Paley, P. Pandey, R. B. Patterson, G. Pawloski, D. Pershey, O. Petrova,  
 1230 R. Petti, S. Phan-Budd, R. K. Plunkett, R. Poling, B. Potukuchi, C. Principato,  
 1231 F. Psihas, A. Radovic, R. A. Rameika, B. Rebel, B. Reed, D. Rocco, P. Rojas,  
 1232 V. Ryabov, K. Sachdev, P. Sail, O. Samoylov, M. C. Sanchez, R. Schroeter,  
 1233 J. Sepulveda-Quiroz, P. Shanahan, A. Sheshukov, J. Singh, J. Singh, P. Singh,  
 1234 V. Singh, J. Smolik, N. Solomey, E. Song, A. Sousa, K. Soustruznik, M. Strait,  
 1235 L. Suter, R. L. Talaga, M. C. Tamsett, P. Tas, R. B. Thayyullathil, J. Thomas,  
 1236 X. Tian, S. C. Tognini, J. Tripathi, A. Tsaris, J. Urheim, P. Vahle, J. Vasel,  
 1237 L. Vinton, A. Vold, T. Vrba, B. Wang, M. Wetstein, D. Whittington, S. G. Wo-  
 1238 jcicki, J. Wolcott, N. Yadav, S. Yang, J. Zalesak, B. Zamorano, and R. Zwaska.  
 1239 Constraints on oscillation parameters from  $\nu_e$  appearance and  $\nu_\mu$  disappearance  
 1240 in nova. *Phys. Rev. Lett.*, 118:231801, Jun 2017.

1241 [13] Alan Agresti. *Categorical Data Analysis*. Wiley Series in Probability and Statis-  
 1242 tics. Wiley, 2013.

1243 [14] A. Aguilar-Arevalo et al. Evidence for neutrino oscillations from the observation  
 1244 of anti-neutrino(electron) appearance in a anti-neutrino(muon) beam. *Phys.*  
 1245 *Rev.*, D64:112007, 2001.

1246 [15] A. A. Aguilar-Arevalo et al. Improved Search for  $\bar{\nu}_\mu \rightarrow \bar{\nu}_e$  Oscillations in the  
 1247 MiniBooNE Experiment. *Phys. Rev. Lett.*, 110:161801, 2013.

1248 [16] S. Amoruso et al. Study of electron recombination in liquid argon with the  
 1249 ICARUS TPC. *Nucl. Instrum. Meth.*, A523:275–286, 2004.

1250 [17] C. Anderson et al. The ArgoNeuT Detector in the NuMI Low-Energy beam  
 1251 line at Fermilab. *JINST*, 7:P10019, 2012.

- [18] C. Andreopoulos et al. The GENIE Neutrino Monte Carlo Generator. *Nucl. Instrum. Meth.*, A614:87–104, 2010.
- [19] Timofei Bolshakov Andrey Petrov. Java synoptic toolkit. Technical report, Sept 2010.
- [20] M. Antonello, B. Baibussinov, P. Benetti, E. Calligarich, N. Canci, S. Centro, A. Cesana, K. Cieslik, D. B. Cline, A. G. Cocco, A. Dabrowska, D. Dequal, A. Dermenev, R. Dolfini, C. Farnese, A. Fava, A. Ferrari, G. Fiorillo, D. Gibin, S. Gninenko, A. Guglielmi, M. Haranczyk, J. Holeczek, A. Ivashkin, J. Kisiel, I. Kochanek, J. Lagoda, S. Mania, A. Menegolli, G. Meng, C. Montanari, S. Otwinowski, A. Piazzoli, P. Picchi, F. Pietropaolo, P. Plonski, A. Rappoldi, G. L. Raselli, M. Rossella, C. Rubbia, P. Sala, A. Scaramelli, E. Segreto, F. Sergiampietri, D. Stefan, J. Stepaniak, R. Sulej, M. Szarska, M. Terani, F. Varanini, S. Ventura, C. Vignoli, H. Wang, X. Yang, A. Zalewska, and K. Zaremba. Precise 3d track reconstruction algorithm for the ICARUS t600 liquid argon time projection chamber detector. *Advances in High Energy Physics*, 2013:1–16, 2013.
- [21] M. Antonello et al. A Proposal for a Three Detector Short-Baseline Neutrino Oscillation Program in the Fermilab Booster Neutrino Beam. 2015.
- [22] D. Ashery, I. Navon, G. Azuelos, H. K. Walter, H. J. Pfeiffer, and F. W. Schlepütz. True absorption and scattering of pions on nuclei. *Phys. Rev. C*, 23:2173–2185, May 1981.
- [23] C. Athanassopoulos et al. Evidence for  $\nu(\mu) \rightarrow \nu(e)$  neutrino oscillations from LSND. *Phys. Rev. Lett.*, 81:1774–1777, 1998.

- [24] Borut Bajc, Junji Hisano, Takumi Kuwahara, and Yuji Omura. Threshold corrections to dimension-six proton decay operators in non-minimal {SUSY} su(5) {GUTs}. *Nuclear Physics B*, 910:1 – 22, 2016.
- [25] B. Baller. Trajcluster user guide. Technical report, apr 2016.
- [26] Gary Barker. Neutrino event reconstruction in a liquid argon TPC. *Journal of Physics: Conference Series*, 308:012015, jul 2011.
- [27] BASF Corp. 100 Park Avenue, Florham Park, NJ 07932 USA.
- [28] R. Becker-Szendy, C. B. Bratton, D. R. Cady, D. Casper, R. Claus, M. Crouch, S. T. Dye, W. Gajewski, M. Goldhaber, T. J. Haines, P. G. Halverson, T. W. Jones, D. Kielczewska, W. R. Kropp, J. G. Learned, J. M. LoSecco, C. McGrew, S. Matsuno, J. Matthews, M. S. Mudah, L. Price, F. Reines, J. Schultz, D. Sinclair, H. W. Sobel, J. L. Stone, L. R. Sulak, R. Svoboda, G. Thornton, and J. C. van der Velde. Search for proton decay into  $e^+ + \pi^0$  in the imb-3 detector. *Phys. Rev. D*, 42:2974–2976, Nov 1990.
- [29] J B Birks. Scintillations from organic crystals: Specific fluorescence and relative response to different radiations. *Proceedings of the Physical Society. Section A*, 64(10):874, 1951.
- [30] A. Bodek and J. L. Ritchie. Further studies of fermi-motion effects in lepton scattering from nuclear targets. *Phys. Rev. D*, 24:1400–1402, Sep 1981.
- [31] Mark G. Boulay and A. Hime. Direct WIMP detection using scintillation time discrimination in liquid argon. 2004.
- [32] D. V. Bugg, R. S. Gilmore, K. M. Knight, D. C. Salter, G. H. Stafford, E. J. N. Wilson, J. D. Davies, J. D. Dowell, P. M. Hattersley, R. J. Homer, A. W. O’dell,

1298 A. A. Carter, R. J. Tapper, and K. F. Riley. Kaon-nucleon total cross sections  
1299 from 0.6 to 2.65 gev/ *c. Phys. Rev.*, 168:1466–1475, Apr 1968.

1300 [33] W. M. Burton and B. A. Powell. Fluorescence of tetraphenyl-butadiene in the  
1301 vacuum ultraviolet. *Applied Optics*, 12(1):87, jan 1973.

1302 [34] CAEN. Caen v1495 data sheet. Technical report, jan 2018.

1303 [35] CAEN. Caen v1740 data sheet. Technical report, jan 2018.

1304 [36] A. S. Carroll, I. H. Chiang, C. B. Dover, T. F. Kycia, K. K. Li, P. O. Mazur,  
1305 D. N. Michael, P. M. Mockett, D. C. Rahm, and R. Rubinstein. Pion-nucleus  
1306 total cross sections in the (3,3) resonance region. *Phys. Rev. C*, 14:635–638,  
1307 Aug 1976.

1308 [37] D. Casper. The nuance neutrino physics simulation, and the future. *Nuclear*  
1309 *Physics B - Proceedings Supplements*, 112(1-3):161–170, nov 2002.

1310 [38] A. Cervera, A. Donini, M.B. Gavela, J.J. Gomez Cádenas, P. Hernández,  
1311 O. Mena, and S. Rigolin. Golden measurements at a neutrino factory. *Nu-*  
1312 *clear Physics B*, 579(1-2):17–55, jul 2000.

1313 [39] E. Church. LArSoft: A Software Package for Liquid Argon Time Projection  
1314 Drift Chambers. 2013.

1315 [40] ATLAS Collaboration. Observation of a new particle in the search for the  
1316 standard model higgs boson with the ATLAS detector at the LHC. *Physics*  
1317 *Letters B*, 716(1):1–29, sep 2012.

1318 [41] CMS Collaboration. Observation of a new boson at a mass of 125 gev with the  
1319 cms experiment at the lhc. *Physics Letters B*, 716(1):30 – 61, 2012.

1320 [42] The LArIAT Collaboration. The liquid argon in a testbeam (lariat) experiment.  
1321 Technical report, In Preparation 2018.

- [43] Stefano Dell’Oro, Simone Marcocci, Matteo Viel, and Francesco Vissani. Neutrinoless double beta decay: 2015 review. *Advances in High Energy Physics*, 2016:1–37, 2016.
- [44] S.E. Derenzo, A.R. Kirschbaum, P.H. Eberhard, R.R. Ross, and F.T. Solmitz. Test of a liquid argon chamber with 20 m rms resolution. *Nuclear Instruments and Methods*, 122:319 – 327, 1974.
- [45] Savas Dimopoulos, Stuart Raby, and Frank Wilczek. Proton Decay in Supersymmetric Models. *Phys. Lett.*, B112:133, 1982.
- [46] D. Drakoulakos et al. Proposal to perform a high-statistics neutrino scattering experiment using a fine-grained detector in the NuMI beam. 2004.
- [47] A Ereditato, C C Hsu, S Janos, I Kreslo, M Messina, C Rudolf von Rohr, B Rossi, T Strauss, M S Weber, and M Zeller. Design and operation of argontube: a 5 m long drift liquid argon tpc. *Journal of Instrumentation*, 8(07):P07002, 2013.
- [48] Torleif Ericson and Wolfram Weise. *Pions and Nuclei (The International Series of Monographs on Physics)*. Oxford University Press, 1988.
- [49] A.A. Aguilar-Arevalo et al. The miniboone detector. *Nuclear Instruments and Methods in Physics Research Section A: Accelerators, Spectrometers, Detectors and Associated Equipment*, 599(1):28 – 46, 2009.
- [50] Antonio Bueno et al. Nucleon decay searches with large liquid argon TPC detectors at shallow depths: atmospheric neutrinos and cosmogenic backgrounds. *Journal of High Energy Physics*, 2007(04):041–041, apr 2007.
- [51] A.S. Clough et al. Pion-nucleus total cross sections from 88 to 860 MeV. *Nuclear Physics B*, 76(1):15–28, jul 1974.

- [52] B.W. Allardyce et al. Pion reaction cross sections and nuclear sizes. *Nuclear Physics A*, 209(1):1 – 51, 1973.
- [53] C Athanassopoulos et al. The liquid scintillator neutrino detector and LAMPF neutrino source. *Nuclear Instruments and Methods in Physics Research Section A: Accelerators, Spectrometers, Detectors and Associated Equipment*, 388(1-2):149–172, mar 1997.
- [54] F. Binon et al. Scattering of negative pions on carbon. *Nuclear Physics B*, 17(1):168 – 188, 1970.
- [55] L. Aliaga et al. Minerva neutrino detector response measured with test beam data. *Nuclear Instruments and Methods in Physics Research Section A: Accelerators, Spectrometers, Detectors and Associated Equipment*, 789:28 – 42, 2015.
- [56] M Adamowski et al. The liquid argon purity demonstrator. *Journal of Instrumentation*, 9(07):P07005, 2014.
- [57] P. Vilain et al. Coherent single charged pion production by neutrinos. *Physics Letters B*, 313(1-2):267–275, aug 1993.
- [58] R. Acciarri et al. Convolutional neural networks applied to neutrino events in a liquid argon time projection chamber. *Journal of Instrumentation*, 12(03):P03011, 2017.
- [59] R. Acciarri et al. Design and construction of the MicroBooNE detector. *Journal of Instrumentation*, 12(02):P02017–P02017, feb 2017.
- [60] C. E. Aalseth et al. DarkSide-20k: A 20 tonne two-phase LAr TPC for direct dark matter detection at LNGS. *The European Physical Journal Plus*, 133(3), mar 2018.

- 1370 [61] H Fenker. Standard beam pwc for fermilab. Technical report, Fermi National  
1371 Accelerator Lab., Batavia, IL (USA), 1983.
- 1372 [62] H Fesbach. Theoretical nuclear physics: Nuclear reactions. 1992.
- 1373 [63] J. A. Formaggio and G. P. Zeller. From ev to eev: Neutrino cross sections across  
1374 energy scales. *Rev. Mod. Phys.*, 84:1307–1341, Sep 2012.
- 1375 [64] E. Friedman et al. K+ nucleus reaction and total cross-sections: New analysis  
1376 of transmission experiments. *Phys. Rev.*, C55:1304–1311, 1997.
- 1377 [65] V.M. Gehman, S.R. Seibert, K. Rielage, A. Hime, Y. Sun, D.-M. Mei,  
1378 J. Maassen, and D. Moore. Fluorescence efficiency and visible re-emission  
1379 spectrum of tetraphenyl butadiene films at extreme ultraviolet wavelengths.  
1380 *Nuclear Instruments and Methods in Physics Research Section A: Accelerators,*  
1381 *Spectrometers, Detectors and Associated Equipment*, 654(1):116 – 121, 2011.
- 1382 [66] H. Geiger and E. Marsden. On a diffuse reflection of the formula-particles.  
1383 *Proceedings of the Royal Society A: Mathematical, Physical and Engineering*  
1384 *Sciences*, 82(557):495–500, jul 1909.
- 1385 [67] Howard Georgi and S. L. Glashow. Unity of all elementary-particle forces. *Phys.*  
1386 *Rev. Lett.*, 32:438–441, Feb 1974.
- 1387 [68] D.Y. Wong (editor) G.L. Shaw (Editor). *Pion-nucleon Scattering*. John Wiley  
1388 & Sons Inc, 1969.
- 1389 [69] Glassman High Voltage, Inc., Precision Regulated High Voltage DC Power Sup-  
1390 ply.
- 1391 [70] D S Gorbunov. Sterile neutrinos and their role in particle physics and cosmology.  
1392 *Physics-Uspekhi*, 57(5):503, 2014.

- [71] C. Green, J. Kowalkowski, M. Paterno, M. Fischler, L. Garren, and Q. Lu. The Art Framework. *J. Phys. Conf. Ser.*, 396:022020, 2012.
- [72] S. Hansen, D. Jensen, G. Savage, E. Skup, and A. Soha. Fermilab test beam multi-wire proportional chamber tracking system upgrade. June 2014. International Conference on Technology and Instrumentation in Particle Physics (TIPP 2014).
- [73] J. Harada. Non-maximal  $\theta_{23}$  , large  $\theta_{13}$  and tri-bimaximal  $\theta_{12}$  via quark-lepton complementarity at next-to-leading order. *EPL (Europhysics Letters)*, 103(2):21001, 2013.
- [74] Peter W. Higgs. Broken symmetries and the masses of gauge bosons. *Physical Review Letters*, 13(16):508–509, oct 1964.
- [75] P.W. Higgs. Broken symmetries, massless particles and gauge fields. *Physics Letters*, 12(2):132–133, sep 1964.
- [76] H J Hilke. Time projection chambers. *Reports on Progress in Physics*, 73(11):116201, 2010.
- [77] N. Ishida, M. Chen, T. Doke, K. Hasuike, A. Hitachi, M. Gaudreau, M. Kase, Y. Kawada, J. Kikuchi, T. Komiyama, K. Kuwahara, K. Masuda, H. Okada, Y.H. Qu, M. Suzuki, and T. Takahashi. Attenuation length measurements of scintillation light in liquid rare gases and their mixtures using an improved reflection suppresser. *Nuclear Instruments and Methods in Physics Research Section A: Accelerators, Spectrometers, Detectors and Associated Equipment*, 384(2-3):380–386, jan 1997.
- [78] G. Pulliam J. Asaadi, E. Gramellini. Determination of the electron lifetime in lariat. Technical report, August 2017.



- 1417 [79] George Jaffé. Zur theorie der ionisation in kolonnen. *Annalen der Physik*,  
1418 347(12):303–344, 1913.
- 1419 [80] C. Jarlskog. A basis independent formulation of the connection between quark  
1420 mass matrices, CP violation and experiment. *Zeitschrift für Physik C Particles  
1421 and Fields*, 29(3):491–497, sep 1985.
- 1422 [81] B J P Jones, C S Chiu, J M Conrad, C M Ignarra, T Katori, and M Toups. A  
1423 measurement of the absorption of liquid argon scintillation light by dissolved ni-  
1424 trogen at the part-per-million level. *Journal of Instrumentation*, 8(07):P07011,  
1425 2013.
- 1426 [82] Benjamin J. P. Jones. *Sterile Neutrinos in Cold Climates*. PhD thesis, MIT,  
1427 2015.
- 1428 [83] Cezary Juszczak, Jarosław A. Nowak, and Jan T. Sobczyk. Simulations from  
1429 a new neutrino event generator. *Nuclear Physics B - Proceedings Supplements*,  
1430 159:211–216, sep 2006.
- 1431 [84] D. I. Kazakov. Beyond the standard model: In search of supersymmetry. In  
1432 *2000 European School of high-energy physics, Caramulo, Portugal, 20 Aug-2  
1433 Sep 2000: Proceedings*, pages 125–199, 2000.
- 1434 [85] Dae-Gyu Lee, R. N. Mohapatra, M. K. Parida, and Merostar Rani. Predic-  
1435 tions for the proton lifetime in minimal nonsupersymmetric so(10) models: An  
1436 update. *Phys. Rev. D*, 51:229–235, Jan 1995.
- 1437 [86] M A Leigui de Oliveira. Expression of Interest for a Full-Scale Detector Engi-  
1438 neering Test and Test Beam Calibration of a Single-Phase LAr TPC. Technical  
1439 Report CERN-SPSC-2014-027. SPSC-EOI-011, CERN, Geneva, Oct 2014.

- 1440 [87] W. H. Lippincott, K. J. Coakley, D. Gastler, A. Hime, E. Kearns, D. N. McK-  
1441 insey, J. A. Nikkel, and L. C. Stonehill. Scintillation time dependence and pulse  
1442 shape discrimination in liquid argon. *Phys. Rev. C*, 78:035801, Sep 2008.
- 1443 [88] Jorge L. Lopez and Dimitri V. Nanopoulos. Flipped SU(5): Origins and re-  
1444 cent developments. In *15th Johns Hopkins Workshop on Current Problems*  
1445 *in Particle Theory: Particle Physics from Underground to Heaven Baltimore,*  
1446 *Maryland, August 26-28, 1991*, pages 277–297, 1991.
- 1447 [89] Vincent Lucas and Stuart Raby. Nucleon decay in a realistic so(10) susy gut.  
1448 *Phys. Rev. D*, 55:6986–7009, Jun 1997.
- 1449 [90] Ettore Majorana. Teoria simmetrica dell’elettrone e del positrone. *Il Nuovo*  
1450 *Cimento*, 14(4):171–184, apr 1937.
- 1451 [91] Hisakazu Minakata and Alexei Yu. Smirnov. Neutrino mixing and quark-lepton  
1452 complementarity. *Phys. Rev. D*, 70:073009, Oct 2004.
- 1453 [92] M. Mooney. The microboone experiment and the impact of space charge effects.  
1454 2015.
- 1455 [93] E. Morikawa, R. Reininger, P. Görtler, V. Saile, and P. Laporte. Argon, kryp-  
1456 ton, and xenon excimer luminescence: From the dilute gas to the condensed  
1457 phase. *The Journal of Chemical Physics*, 91(3):1469–1477, aug 1989.
- 1458 [94] FM Newcomer, S Tedja, R Van Berg, J Van der Spiegel, and HH Williams.  
1459 A fast, low power, amplifier-shaper-discriminator for high rate straw tracking  
1460 systems. *IEEE Transactions on Nuclear Science*, 40(4):630–636, 1993.
- 1461 [95] Emmy Noether. Invariant variation problems. *Transport Theory and Statistical*  
1462 *Physics*, 1(3):186–207, jan 1971.

- 1463 [96] I. Nutini. Study of charged particles interaction processes on ar in the 0.2 - 2.0  
1464 GeV energy range through combined information from ionization free charge  
1465 and scintillation light. Technical report, jan 2015.
- 1466 [97] D. R. Nygren. The time projection chamber: A new 4  $\pi$  detector for charged  
1467 particles. Technical report, 1974.
- 1468 [98] L. Onsager. Initial recombination of ions. *Phys. Rev.*, 54:554–557, Oct 1938.
- 1469 [99] S. Pascoli, S.T. Petcov, and A. Riotto. Leptogenesis and low energy cp-violation  
1470 in neutrino physics. *Nuclear Physics B*, 774(1):1 – 52, 2007.
- 1471 [100] C. Patrignani et al. Review of Particle Physics. *Chin. Phys.*, C40(10):100001,  
1472 2016.
- 1473 [101] B. Pontecorvo. Neutrino Experiments and the Problem of Conservation of  
1474 Leptonic Charge. *Sov. Phys. JETP*, 26:984–988, 1968. [Zh. Eksp. Teor.  
1475 Fiz.53,1717(1967)].
- 1476 [102] T. Yang R. Acciarri. Investigation of the non-uniformity observed in the wire  
1477 response to charge in lariat run 1. Technical report, February 2017.
- 1478 [103] T. Yang R. Acciarri, M. Stancari. Determination of the electron lifetime in  
1479 lariat. Technical report, March 2016.
- 1480 [104] Martti Raidal. Relation between the neutrino and quark mixing angles and  
1481 grand unification. *Phys. Rev. Lett.*, 93:161801, Oct 2004.
- 1482 [105] Steve Ritz et al. Building for Discovery: Strategic Plan for U.S. Particle Physics  
1483 in the Global Context. 2014.
- 1484 [106] C. Rubbia. The Liquid Argon Time Projection Chamber: A New Concept for  
1485 Neutrino Detectors. 1977.

- 1486 [107] L.M. Saunders. Electromagnetic production of pions from nuclei. *Nucl. Phys.*,  
1487 *B7: 293-310(1968)*.
- 1488 [108] Qaisar Shafi and Zurab Tavartkiladze. Neutrino democracy, fermion mass hier-  
1489 archies, and proton decay from 5d su(5). *Phys. Rev. D*, 67:075007, Apr 2003.
- 1490 [109] Sigma-Aldrich, P.O. Box 14508, St. Louis, MO 63178 USA.
- 1491 [110] R. K. Teague and C. J. Pings. Refractive index and the lorentz-lorenz function  
1492 for gaseous and liquid argon, including a study of the coexistence curve near the  
1493 critical state. *The Journal of Chemical Physics*, 48(11):4973–4984, jun 1968.
- 1494 [111] J. Thomas and D. A. Imel. Recombination of electron-ion pairs in liquid argon  
1495 and liquid xenon. *Phys. Rev. A*, 36:614–616, Jul 1987.
- 1496 [112] D.R.O. Morrison N. Rivoire V. Flaminio, W.G. Moorhead. Compilation of  
1497 Cross Sections I:  $\pi^+$  and  $\pi^-$  Induced Reactions. *CERN-HERA*, pages 83–01,  
1498 1983.
- 1499 [113] D.R.O. Morrison N. Rivoire V. Flaminio, W.G. Moorhead. Compilation of  
1500 Cross Sections II:  $K^+$  and  $K^-$  Induced Reactions. *CERN-HERA*, pages 83–02,  
1501 1983.
- 1502 [114] Hermann Weyl. Gravitation and the electron. *Proceedings of the National*  
1503 *Academy of Sciences of the United States of America*, 15(4):323–334, 1929.
- 1504 [115] Colin et al Wilkin. A comparison of pi+ and pi- total cross-sections of light  
1505 nuclei near the 3-3 resonance. *Nucl. Phys.*, B62:61–85, 1973.
- 1506 [116] D. H. Wright and M. H. Kelsey. The Geant4 Bertini Cascade. *Nucl. Instrum.*  
1507 *Meth.*, A804:175–188, 2015.

- 1508 [117] C. S. Wu, E. Ambler, R. W. Hayward, D. D. Hoppes, and R. P. Hudson.  
1509 Experimental test of parity conservation in beta decay. *Phys. Rev.*, 105:1413–  
1510 1415, Feb 1957.
- 1511 [118] N Yahlali, L M P Fernandes, K Gonzlez, A N C Garcia, and A Soriano. Imaging  
1512 with sipms in noble-gas detectors. *Journal of Instrumentation*, 8(01):C01003,  
1513 2013.
- 1514 [119] T. Yanagida. Horizontal symmetry and masses of neutrinos. *Progress of Theo-*  
1515 *retical Physics*, 64(3):1103–1105, sep 1980.